Pulsed Magnetic Imaging of Broad-Frequency Fields using Nitrogen-Vacancy Centers in Diamond

by

Samuel Karlson

B.S., United States Air Force Academy (2022)

Submitted to the Department of Nuclear Science and Engineering
in partial fulfillment of the requirements for the degree
of
Master of Nuclear Science and Engineering

at the

MASSACHUSETTS INSTITUTE OF TECHNOLOGY

May 2024

Authored by: Samuel Karlson
Department of Nuclear Science and Engineering
May 15, 2024

Certified by: Paola Cappellaro
Ford Professor of Nuclear Science and Engineering and Professor of Physics
Thesis Supervisor

Certified by: Danielle Braje
Associate Group Leader, Quantum Information and Integrated Nanosystems, MIT Lincoln Laboratories
Thesis Supervisor

Accepted by: Ju Li
Department of Nuclear Science and Engineering
Chair, Department Committee on Graduate Theses

Pulsed Magnetic Imaging of Broad-Frequency Fields using Nitrogen-Vacancy Centers in Diamond

by

Samuel Karlson

Submitted to the Department of Nuclear Science and Engineering
on May 15, 2024, in partial fulfillment of the
requirements for the degree of
Master of Nuclear Science and Engineering

Abstract

Wide-field magnetic imaging using nitrogen-vacancy (NV) centers in diamond can yield high-quality images for various applications, including biology, geology, condensed-matter physics, and electronics troubleshooting. These quantum sensors yield wide-field-of-view images with micron-scale spatial resolution and operate in ambient conditions. Most of the sensing work with NV centers in diamond has focused on DC and low frequency AC fields. This thesis demonstrates a wide-field magnetic imager and its capabilities with test structures of varying complexity. We overcome the challenges for measuring MHz frequency magnetic fields with a quantum frequency mixing approach.

Thesis Supervisor: Paola Cappellaro
Title: Ford Professor of Nuclear Science and Engineering and Professor of Physics

Thesis Supervisor: Danielle Braje
Title: Associate Group Leader, Quantum Information and Integrated Nanosystems, MIT Lincoln Laboratories

Acknowledgments

I would like to thank the following people for their help and support. In addition to their immense service in teaching me and guiding me in the lab, I appreciate their humor, fun spirits, and unique personalities. The following quotes are just a few of my favorite expressions from the incredible people that I worked with at Lincoln Laboratories:

"Ok" - Dr. Pauli Kehayias
"Science is hard" - Dr. Pauli Kehayias
"Fine" - Dr. Matthew Steinecker
"Fine" - Dr. Jenny Schloss, imitating Matt
"Everything always comes back to the Bloch Sphere" - Dr. Jenny Schloss, spinning her thumbs in circles
"If you're not breaking things once in a while, you're not working hard enough" - Dr. Jenny Schloss
"You should always be skeptical of everything I say" - Dr. David Phillips
"You should always be skeptical of everything Matt says" - Reggie Wilcox
"Let me tell you about..." - Dr. Matthew Steinecker
"The lab fairies keep stealing our tools" - Andrew Maccabe
"I really need to do this paperwork... but lab time sounds like SOOO much more fun" - Andrew Maccabe
"It feels like it should be Friday" - Dr. Danielle Braje, at Monday morning student group meeting
"There are lots of cool things you can do with diamonds on the moon" - Dr. Danielle Braje

Thank you Danielle, for building a team atmosphere that feels more like family than co-workers. Thank you Andrew, for showing me what it means to be an engineer. Thank you Pauli, for showing me what it means to be a scientist. Thank you Jenny,

for putting everything about this initially crazy-seeming experiment in the context of something I could understand with incredible patience and kindness. Thank you David, for reminding me that it's always ok to ask for help. Thank you Reggie, for answering a million questions, including if all food is a soup, salad, or sandwich. Thank you Matt, for helping me remember that research should be fun.

I would also like to thank all of the members of the MIT Quantum Engineering Group. I am grateful for the many group meetings on campus filled with jokes, snacks, and interesting presentations. I am grateful for the lab tours, social outings and dinners. I am grateful for the many nights spent working together on homework for 8.511 and 22.51. Thank you Alex, Andrew, Takuya, Santiago, Boning, Minh-Thi, Garrett, and Jungbae. I am grateful for Guoqing, whose work with quantum frequency mixing created the basis for this thesis. Thank you for spending time and time again helping me understand your work, and thank you for your friendship. Thank you Paola, for your immense patience, kindness, and uplifting nature as both a professor and advisor.

Last of all, thank you to my family, for your constant love and support.

Disclaimer

This material is based upon work supported by the Under Secretary of Defense for Research and Engineering under Air Force Contract No. FA8702-15-D-0001. Any opinions, findings, conclusions or recommendations expressed in this material are those of the author(s) and do not necessarily reflect the views of the Under Secretary of Defense for Research and Engineering.

Contents

1 Nitrogen-Vacancy Centers in Diamond for Wide-field Magnetic Imaging **15**

1.1 Introduction 15

1.2 Motivation 16

1.3 Theory of Nitrogen-Vacancy Centers in Diamond 17

1.4 Nitrogen-Vacancy Center Hamiltonian 19

2 Quantum Sensing Protocols **21**

2.1 Quantum Sensing Protocol 21

2.2 Interaction Picture 22

2.3 Rabi Magnetometry 23

2.4 Ramsey Magnetometry 26

2.5 Quantum Frequency Mixed Rabi 27

3 Wide-field Magnetic Imaging **33**

3.1 Nitrogen-Vacancy Magnetic Imager Concept 33

3.2 Experimental Methods for Imaging 35

3.3 Experimental Ramsey Pulse Sequence 35

3.4 Through-Silicon Via Test Chip at DC 40

4 Quantum Frequency Mixing on an Imager **45**

4.1 Experimental Quantum Frequency Mixing Pulse Sequence 45

4.2 Test Structures 46

4.3 Results . . . 48
4.3.1 Initial Validation . . . 48
4.3.2 Strong-Drive, Low Signal Frequency Regimes . . . 50
4.3.3 Weak-Drive Regimes . . . 51

5 Imaging AC fields in Fabricated Devices **53**
5.1 Archimedes Spiral Structure . . . 53
5.2 Through-Silicon Via Test Chip at AC Frequencies . . . 56

6 Conclusion and Outlook **59**

A Magnetic Imager Noise and Resolution **61**
A.1 Spatial Magnetic Noise Floor and Noise Subtraction Protocol . . . 61
A.2 Resolution . . . 65
A.2.1 Spatial Resolution . . . 65
A.2.2 Temporal Resolution . . . 66

B Magnetic Imager Experimental Setup **69**
B.1 Magnetic Imager Optical Path . . . 69
B.2 Static Bias Magnetic Field . . . 71
B.3 Experiment Pulse Sequences . . . 72
B.4 Electronics . . . 73
B.4.1 Acousto-Optic Modulator Electronics . . . 73
B.4.2 Microwave Electronics . . . 74
B.4.3 Signal Electronics . . . 75
B.4.4 Arbitrary Waveform Generator Setup Summary . . . 76
B.4.5 Electronics Components List . . . 77

List of Figures

1-1 Schematic of a nitrogen-vacancy center in a diamond lattice 18

1-2 Energy levels of a negatively charged nitrogen-vacancy center 19

2-1 Rabi pulse sequence 25

2-2 Rabi oscillations 25

2-3 Visual of quantum frequency mixing 29

3-1 Schematic diagram of a nitrogen-vacancy center diamond magnetic imager 34

3-2 Visual depiction of linear detection for a Ramsey experiment 36

3-3 Pulse sequence steps for performing Ramsey magnetometry 39

3-4 Optical image and schematic of through-silicon via test structure . . . 41

3-5 Magnetic field image of through-silicon via test structure 42

3-6 Magnetic movie 43

4-1 Schematic diagram of quantum frequency mixing on a magnetic imager 46

4-2 Comparison of pulse sequences used to validate quantum frequency mixing 47

4-3 Validation of quantum frequency mixing using a straight wire test structure 49

4-4 Numerical simulation demonstrating where quantum frequency mixing scaling law matches theory across different signal frequencies 52

4-5 Numerical simulation showing where quantum frequency mixing scaling law matches theory across different signal amplitudes 52

5-1 Application of quantum frequency mixing for imaging a spiral test structure 55
5-2 Application of quantum frequency mixing for imaging a through-silicon via test chip 57

A-1 Visual depiction of background noise subtraction scheme for Rabi measurements 62
A-2 Spatial magnetic noise floor as a function of acquisition time for DC imaging 65
A-3 Meander test structure for characterizing spatial resolution of the imager 66

B-1 Block diagram showing the excitation optical path 70
B-2 Bias magnets aligned along one of the nitrogen-vacancy center axes used to break zero-field degeneracy 71
B-3 Schematic of electronics used to control the acousto-optic modulator . 73
B-4 Schematic of the electronics used to deliver microwaves to the diamond 74
B-5 Schematic of the electronics used to deliver the sensing signal to the test structure 75

List of Tables

B.1 Table summarizing what section of the experiment each channel of the arbitrary waveform generator controls 76

B.2 List of electronics components used to implement the pulse sequences and microwave delivery for the magnetic imager 77

Chapter 1

Nitrogen-Vacancy Centers in Diamond for Wide-field Magnetic Imaging

1.1 Introduction

A magnetometer is a device that measures a magnetic field. Quantum sensors have gained significant attention for their capabilities as high sensitivity magnetometers, historically in atomic magnetometers and more recently using solid state defects such as nitrogen-vacancy (NV) centers in diamond. A quantum sensor utilizes properties of quantum mechanics (such as quantized energy levels, quantum coherence, or quantum entanglement) to observe a phenomenon [1]. Examples of quantum sensors used for magnetometry include neutral atoms, atomic vapors, superconducting quantum interference devices (SQUIDs), and NV centers in diamond [1, 2]. NV centers in diamond are promising quantum sensors because they operate over a wide temperature range from room temperature to cryogenic temperatures, have long electronic spin lifetimes, and are capable of sensing vector magnetic fields [3]. Moreover, because each NV center is fixed in the lattice, NV centers in diamond are capable of spatially resolved imaging. Both single NV centers and NV ensembles are used for magnetic

imaging. NV ensembles for wide-field imaging have the ability to acquire an image without sensor scanning, enabling the acquisition of spatio-temporal dynamics while still offering micron-scale spatial resolution [4, 5]. This thesis focuses on the wide-field magnetic imaging capabilities of ensemble NV centers in diamond.

1.2 Motivation

High-resolution wide-field magnetic imaging using NV centers has been demonstrated for a wide range of interdisciplinary applications in geology, biology, condensed-matter physics, and electronics [5, 6, 7]. With a few exceptions [8, 9, 10, 11, 12], most NV magnetic imaging experiments have implemented an apparatus sensitive to DC or low-frequency (~ 1 kHz) AC magnetic fields. High-sensitivity imaging of higher frequency AC fields with NV ensembles typically requires more complex apparatuses with pulsed diamond interrogation and gated optical readout. Moreover, these measurements are restricted to specific and often narrow frequency ranges. For example, pulsed dynamical decoupling is limited by NV spin lifetimes and microwave π-pulse durations to typically < 10 MHz [5, 13], while Rabi AC magnetometry senses in a narrow band around the NV spin resonance frequency, usually near $\sim$3 GHz [14]. Though application of a strong bias magnetic field can offer tunable-frequency sensitivity over a wider frequency range, bias field requirements are typically impractical. As a result, magnetic imaging demonstrations with NV centers to date have sacrificed frequency range, field of view, or both.

This thesis demonstrates an NV widefield magnetic imaging system that measures both DC and AC magnetic fields up to 70 MHz. To enable this broad-frequency sensitivity, we implement a quantum frequency mixer (QFM) approach recently demonstrated with small NV ensembles on our imager [15]. We first demonstrate pulsed magnetic imaging for sensing DC fields. We then image the AC magnetic fields from a straight wire to confirm that NV AC magnetometry using QFM extends to imaging. After validating simple magnetic images are what was expected, we magnetically image more complex test structures.

This work, which combines a high-performance NV AC magnetometry widefield imager and the QFM AC magnetometry technique, opens the possibility of new high-resolution magnetic microscopy applications, including diagnostics of quantum computing hardware (e.g. ion trap chips), high-resolution power spectrum analysis (PSA) imaging of integrated circuits, and validation of ∼1-100 MHz electrical components (e.g. band-pass filters) [16]. Following this initial demonstration, our anticipated future work includes implementing a "spectrum analyzer imager" (compiling a frequency spectrum for every pixel) and imaging the time-dependent dynamics of a wide variety of electronic devices.

1.3 Theory of Nitrogen-Vacancy Centers in Diamond

A nitrogen-vacancy center in a diamond lattice is an atomic-scale defect composed of a substitutional nitrogen and an adjacent vacancy that have replaced two carbon atoms in the lattice (Fig. 1-1). The two predominant electronic charge states for an NV center are the negatively charged NV^- state and the neutral NV^0 state [17]. This thesis focuses on the negatively charged state NV^-, whose Zeeman-sensitive energy level structure is a natural fit for magnetometry, as shown in Fig. 1-2. This charge state occurs because a nearby nitrogen serves as an electron donor, making a total of six electrons in the NV center that form a system with one unit of spin angular momentum, which can be coupled to both microwave and optical fields. The electronic ground state of the NV^- center is a spin triplet state with a 2.87 GHz zero-field splitting [14]. The electronic spin axis is determined by the nitrogen and vacancy site orientation [18]. Nitrogen has two isotopes, ^{14}N and ^{15}N. For our imager, we use a diamond incorporating mostly ^{15}N, which is preferred because ^{15}NV only has two hyperfine features with a larger splitting between the two resonances, compared to the three hyperfine features of ^{14}N [5]. Unless otherwise specified, all further mentions of NV center will specifically refer to $^{15}NV^-$.

Optical photons with frequencies higher than the NV center's 637 nm zero-phonon line excite transitions between the ground and excited triplet states that preserve the

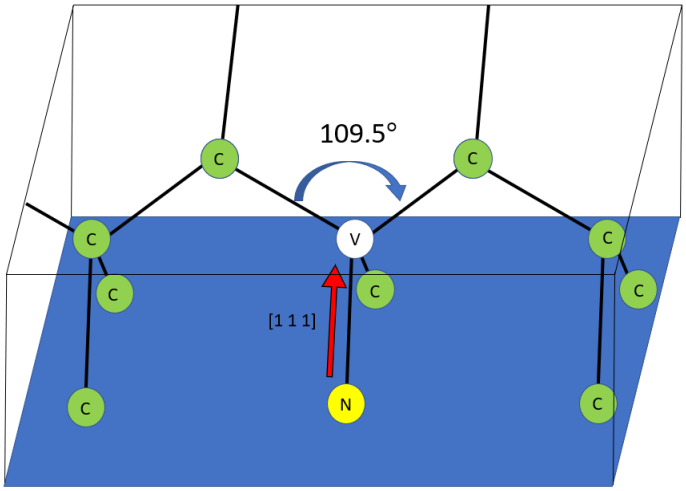

Figure 1-1: Schematic of a nitrogen-vacancy center in a diamond lattice. The NV center as shown is along the [111] crystallographic direction. Two of the carbon atoms have been removed from the lattice and replaced with a single nitrogen atom. Thus, the system is composed of a nitrogen and a "vacancy". For our imager, the diamond is a single crystal chip with a cuboid shape (not drawn to scale). The x and y directions of the crystallographic axes are off-set from the sides of the diamond at a 45 degree angle.

state's spin, and the excited state subsequently decays by emitting fluorescence in the 638-800 nm range. (For optical excitation, 532 nm wavelength is often chosen as a balance of using conveniently available lasers while minimizing excitation of NV^0 centers). The excited triplet states can also return to the ground state through a non-radiative decay pathway via an intersystem crossing, which is preferentially chosen by the $m_s = \pm 1$ states [19, 5]. In addition, this decay pathway does not preserve the spin projection and deposits population in the $m_s = 0$ ground state. As a result, the $m_s = 0$ state is more likely to emit fluorescence, and continual optical excitation results in a higher population in the $m_s = 0$ state. Then, detecting the amount of fluorescence can determine the population of NV centers in each of the $m_s = 0$ and $m_s = \pm 1$ states, which can be reached by applying MW fields. Thus, NV centers can be optically initialized into the $m_s = 0$ quantum state and optically read out through the spin-dependent fluorescence [5, 17].

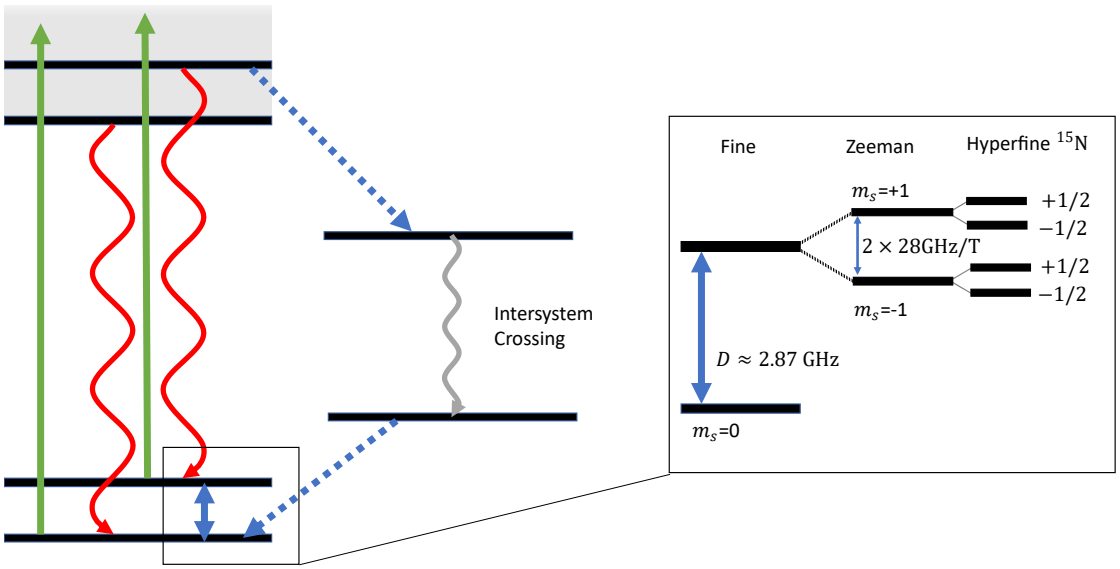

Figure 1-2: Excitation of the $^{15}NV^-$ Center. Optical illumination of the NV center with green light excites the system from the ground to excited electronic state. The excited $m_s = \pm 1$ states are more likely to decay to the ground $m_s = 0$ state through the intersystem crossing. Repetition of this process ensures that the population is primarily in the $m_s = 0$ ground state.

1.4 Nitrogen-Vacancy Center Hamiltonian

The Hamiltonian for the NV center includes dipole-dipole interactions between the two unpaired electrons in the ground state, coupling to any external magnetic fields, interactions with the diamond lattice strain, and hyperfine interaction terms [5, 14]. Since we are not using highly strained diamonds, we can safely neglect the strain and transverse hyperfine interaction terms, since they are relatively small (< 1 MHz) [14, 5, 18, 20]. The resulting Hamiltonian for the NV centers along the NV symmetry axis, which we term the z-axis, is:

$$\frac{H}{\hbar} = DS_z^2 + A_\parallel S_z I_z + \gamma_{\mathrm{NV}} \mathbf{B} \cdot \mathbf{S} \tag{1.1}$$

where H represents the Hamiltonian, $\hbar$ is the reduced Planck's constant, $\mathbf{S}$ and $\mathbf{I}$ are the spin operators for the electron and nuclear spins with S_z and I_z their z-components, $D \approx 2870$ MHz is the zero-field splitting of the NV center, $\mathbf{B}$ is the external magnetic field, $\gamma_{\mathrm{NV}} \approx 28$ GHz/T is the NV center gyromagnetic ratio, and

$A_\parallel \approx 3.0$ MHz is the coupling parameter for the hyperfine splitting [14, 20].

We apply a static bias magnetic field along the NV axis, $\mathbf{B}_0 = B_0\hat{z} \approx 1$ mT, which eliminates the degeneracy between the $m_s = +1$ and $m_s = -1$ levels. If we address the $m_s = 0$ to $m_s = +1$ transition individually (with $m_I = +1/2$), we can treat the resulting Hamiltonian as an effective two-level subspace:

$$H_0 = \hbar \begin{bmatrix} D + \frac{A_\parallel}{2} + \gamma_{\mathrm{NV}} B_0 & 0 \\ 0 & 0 \end{bmatrix}. \tag{1.2}$$

We call $\omega_0 = D + \gamma_{\mathrm{NV}} B_0 + \frac{A_\parallel}{2}$ the natural resonance frequency of the two-level system [14]. Shifting the zero-point of energy to lie half-way between the two levels, the internal Hamiltonian is now

$$H_0 = \frac{\hbar\omega_0}{2}\sigma_z \tag{1.3}$$

where we used the Pauli spin matrix σ_z [14, 20].

Chapter 2

Quantum Sensing Protocols

2.1 Quantum Sensing Protocol

The characteristics of nitrogen-vacancy centers outlined above satisfy three of the requirements necessary to perform quantum sensing as outlined in [1]:

- They have discrete energy levels that can be spectroscopically resolved. (The energy levels are determined by the amount of red fluorescence emitted by the NV centers.)
- They can be initialized into a well-known quantum state. (Optical initialization ensures that the population is primarily in the $m_s = 0$ ground state.)
- There is a physical system that interacts with the quantum system. (When addressing NV centers, this physical system is an external magnetic field applied to the system.)

The final element required to perform quantum sensing is:

- Protocols that coherently control the quantum system.

We will use Rabi and Ramsey magnetometry protocols for our sensor, which will be outlined in the following sections. The generic Hamiltonian for a quantum sensing

protocol includes the internal Hamiltonian of the system, the Hamiltonian of the signal to be sensed, and the Hamiltonian of a control used to tune the sensor. For sensing with NV centers in diamond, which have symmetry axes fixed by the diamond lattice, the signal Hamiltonian is generally split into two components: a component parallel to the NV axis and a component perpendicular to the NV axis [1]. For a quantum sensing protocol using NV centers, the coupling parameter is the NV gyromagnetic ratio $\gamma \approx 28$ GHz/T [20]. The parallel components lead to a shift of the energy levels and thereby the transition frequency, which is what is measured in a Ramsey experiment. The transverse (non-commuting) perturbation induces transitions between levels, which are efficient when on resonance [1]. These transition frequencies are measured in a Rabi protocol.

2.2 Interaction Picture

The interaction picture is used for systems where the evolution of the internal Hamiltonian is easily solvable, but a perturbation V drives dynamics that are unknown.

In the interaction picture, the state $|\psi\rangle$ becomes:

$$|\psi\rangle_I \rightarrow U_0^\dagger(t)\,|\psi\rangle, \tag{2.1}$$

where we use $U_0 = e^{iH_0 t}$, and H_0 is our solvable Hamiltonian [21]. The Hamiltonian in the interaction picture is:

$$H_I(t) \rightarrow U_0^\dagger(t)\,H(t)\,U_0(t) + i\hbar\frac{\partial U_0^\dagger(t)}{\partial t}U_0(t)\,, \tag{2.2}$$

such that the vector state $|\psi\rangle_I$ in the interaction picture evolves according to a Schrodinger's Equation governed by such a Hamiltonian [21, 20]. Any Hermitian operator A in the interaction picture becomes:

$$A \rightarrow U_0^\dagger(t)\,AU_0(t)\,. \tag{2.3}$$

[21]. We can use the interaction picture to solve the Hamiltonian for a system with a

perturbation (i.e. a signal and control Hamiltonian) for which we do not understand the dynamics, such as the Rabi magnetometry protocol described in the following section [21, 20].

2.3 Rabi Magnetometry

For our imager, we utilize a Rabi-based magnetometry scheme. When a two-level system is driven by a resonant magnetic field, the population oscillates between the two states sinusoidally [21]. Rabi driving involves initializing the NV spin state into the $m_s = 0$ state and then applying a microwave (MW) driving field at the resonance frequency to initiate population oscillations. The Rabi frequency is proportional to the amplitude of the MW drive, so detecting the Rabi frequency can be used to determine the strength of the magnetic field [14].

For example, assume we have a static magnetic field along the z-axis that splits the degenerate $m_s = \pm 1$ energy levels of an NV system. If we add an oscillating magnetic field with angular frequency ω along the transverse x direction such that the total magnetic field is given by:

$$\mathbf{B} = B_0 \hat{z} + B_{\mathrm{MW}} \cos(\omega t)\, \hat{x}, \tag{2.4}$$

then the Hamiltonian is a sum of the internal Hamiltonian and the Hamiltonian of the signal field:

$$\frac{H}{\hbar} = \frac{\omega_0}{2}\sigma_z + \Omega \cos(\omega t)\, \sigma_x \tag{2.5}$$

where $\Omega = \gamma B_{\mathrm{MW}}/\sqrt{2}$ for a spin one system [14]. This time-dependent Hamiltonian can be solved using the interaction picture transformation: $U_0 = e^{i(\omega t/2)\sigma_z}$. We use the identities: $e^{i(\omega t/2)\sigma_z}\sigma_x e^{i(\omega t/2)\sigma_z t} = \cos(\omega t)\,\sigma_x + \sin(\omega t)\,\sigma_y$ and $e^{i(\omega t/2)\sigma_z t}\sigma_z e^{i(\omega t/2)\sigma_z t} = \sigma_z$, and the resulting Hamiltonian in the interaction picture is now:

$$\frac{H_I}{\hbar} = \frac{\omega_0}{2}\sigma_z + \frac{\Omega}{2}\left(\sigma_x + \cos(2\omega t)\,\sigma_x + \sin(2\omega t)\,\sigma_y\right) - \frac{\omega}{2}\sigma_z \tag{2.6}$$

where we also used double angle and half angle trigonometric identities. The terms oscillating at a frequency of 2ω will average out during the evolution of the system [14]. This is referred to as the rotating wave approximation. The Hamiltonian in the interaction picture is now time independent:

$$\frac{H_I}{\hbar} = \frac{\delta}{2}\sigma_z + \frac{\Omega}{2}\sigma_x \tag{2.7}$$

where $\delta = \omega - \omega_0$ is the detuning from the driving frequency ω and the resonance frequency ω_0. The evolution of the state in the interaction picture is:

$$|\psi(t)\rangle_I = e^{-iH_I t}|\psi\rangle_I = e^{-i\left(\frac{\delta}{2}\sigma_z + \frac{\Omega}{2}\sigma_x\right)t}|\psi\rangle_I. \tag{2.8}$$

If we start in the $|0\rangle$ state, the probability of flipping to the $|1\rangle$ state is:

$$|\langle 1|\psi(t)\rangle|^2 = \frac{\Omega^2}{\Omega^2 + \delta^2}\sin^2\left(\frac{\sqrt{\Omega^2 + \delta^2}}{2}t\right) \tag{2.9}$$

and when the MW field is on resonance, this becomes

$$|\langle 1|\psi(t)\rangle|^2 = \sin^2\left(\frac{\Omega}{2}t\right) = \frac{1}{2}\left(1 - \cos(\Omega t)\right), \tag{2.10}$$

where t is the total duration of the applied driving field. [14, 21].

For a single NV center, this equation refers to the probability of being in the $m_s = +1$ state at a given time t. For an ensemble of NV centers, this becomes the relative population of NV centers in the $m_s = +1$ state. In practice, camera frame rates inhibit detecting the Rabi oscillations with a continuous MW drive, so to perform a Rabi experiment we initialize the state, apply a MW drive for a fixed duration τ_{Rabi}, read out the state, and then repeat this sequence, varying the duration of τ_{Rabi} as shown in Fig. 2-1. Detecting the frequency of these oscillations can be used to determine the amplitude of the magnetic field as shown in Fig. 2-2. If the MW amplitude is known, Rabi sensing can be used to measure the MW field frequency or the amplitude of an additional DC field, which would manifest as a change in δ from Eq. 2.9 [1, 5].

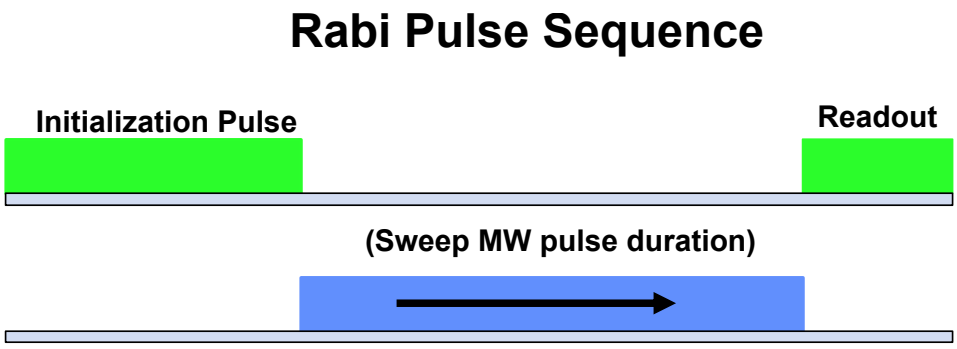

Figure 2-1: Example Rabi pulse sequence. An optical laser pulse initializes the NV centers into the $m_s = 0$ state. A MW pulse is applied that transfers population to the $m_s = +1$ state according to Eq. 2.10. The population is read out using a final optical laser pulse. The sequence is repeated with an increased value of τ, the length of time of the MW pulse.

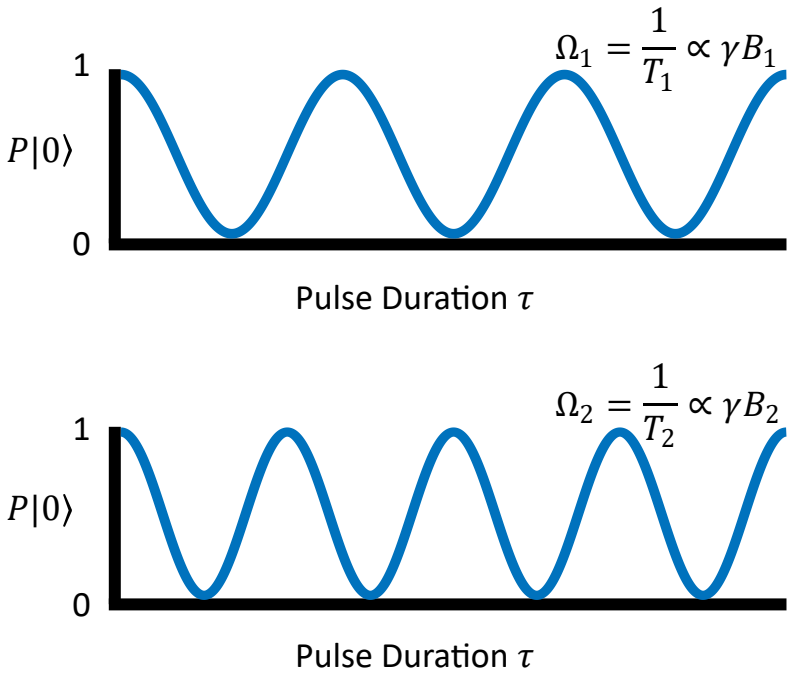

Figure 2-2: Visual demonstration of Rabi oscillations. The length of the MW pulse is swept in time, and the probability of being in either the $m_s = 0$ or $m_s = +1$ state oscillates according to Eq. 2.10. If the magnitude of the magnetic field changes, then the period T of this probability oscillation will also change. By determining the frequency of the Rabi oscillations Ω, the magnitude of the applied magnetic field B can also be determined.

2.4 Ramsey Magnetometry

In order to measure static magnetic fields (produced by direct current) and broadband kHz magnetic fields, we use a Ramsey protocol [5, 22]. In a Ramsey protocol, we apply a resonant MW drive field as the control, and the DC field to be sensed is the perturbation. Instead of sweeping the duration of the MW pulse, Ramsey spectroscopy applies a "$\pi/2$" pulse which creates a superposition of the $m_s = 0$ and $m_s = +1$ states: $|\psi\rangle = \frac{1}{\sqrt{2}}|0\rangle + \frac{1}{\sqrt{2}}|1\rangle$. When the system is in this superposition state, it evolves for a free precession time under the perturbation $H_V = \frac{\gamma B_{\mathrm{DC}}}{2}\sigma_z$. The superposition state accumulates a relative phase proportional to the applied magnetic field, and then an additional $\pi/2$ pulse maps the accumulated phase to relative populations of $m_s = 0$ and $m_s = +1$ states [20].

For example, to create the $\pi/2$ pulse, we start with the lab frame Hamiltonian:

$$\frac{H}{\hbar} = \frac{\omega_0}{2}\sigma_z + \frac{\gamma B_{\mathrm{DC}}}{2}\sigma_z + \Omega\cos(\omega t)\,\sigma_x \tag{2.11}$$

where the Ω term is the same MW drive as the Rabi scheme. We assume this driving field is much larger than the sensing field and temporarily ignore H_V. The Hamiltonian in the interaction picture then becomes like the Rabi scheme above:

$$\frac{H_I}{\hbar} = \frac{\delta}{2}\sigma_z + \frac{\Omega}{2}\sigma_x \tag{2.12}$$

and the system undergoes Rabi oscillations with Rabi frequency Ω. The MW drive is turned off after a time $\tau_{\mathrm{Rabi}} = \pi/(2\Omega)$ which represents a 90 degree or "$\pi/2$" rotation about the x-axis of the Bloch sphere and places the state in an equal superposition state. With the MW drive off, we include the signal perturbation and the Hamiltonian is now (assuming we are on resonance):

$$\frac{H_I}{\hbar} = \frac{\gamma B_{\mathrm{DC}}}{2}\sigma_z. \tag{2.13}$$

The evolution becomes:

$$|\psi\left(\tau_{\pi/2}+\tau_{\text{Ramsey}}\right)\rangle = e^{-i\left(\gamma B_{\text{DC}}\tau_{\text{Ramsey}}/2\right)\sigma_z}|\psi\left(\tau_{\pi/2}\right)\rangle = \frac{1}{\sqrt{2}}\left(e^{-i\frac{\phi}{2}}|0\rangle - i(e^{i\frac{\phi}{2}})|1\rangle\right) \tag{2.14}$$

where we allow the system to evolve for a free precession time τ_{Ramsey} and the state accumulates a phase:

$$\phi = \gamma B_{\text{DC}}\tau_{\text{Ramsey}}. \tag{2.15}$$

Another $\pi/2$ pulse maps the accumulated phase information back to a population difference:

$$|\psi\left(t_{\text{total}}\right)\rangle = e^{-i\frac{\pi}{4}\sigma_x}\left(\frac{1}{\sqrt{2}}\left(e^{-i\frac{\phi}{2}}|0\rangle - i(e^{i\frac{\phi}{2}})|1\rangle\right)\right) \tag{2.16}$$

and the population difference is detected by measuring the spin-projection operator S_z:

$$\langle S_z\rangle = \frac{\hbar}{2}\langle\psi\left|\sigma_z\right|\psi\rangle = \frac{\hbar}{2}\left(\cos^2\left(\frac{\phi}{2}\right) - \sin^2\left(\frac{\phi}{2}\right)\right) = \frac{\hbar}{2}\cos\left(\phi\right) \tag{2.17}$$

which for NV centers in diamond is read out as change in the optical fluorescence [14, 20, 21]. Thus, a change in the magnetic field induces a change in the phase, which results in a cosinusoidal change in the fluorescence.

2.5 Quantum Frequency Mixed Rabi

The Ramsey sequence in the previous section measures static fields or low-AC frequency fields while the Rabi sequence described in Sec. 2.3 induces Rabi oscillations when the MW field is on resonance ω_0, which for our NV system is in the ~2.87 GHz range. In order to measure signal fields outside of these limited ranges, we apply quantum frequency mixing.

A quantum frequency mixer applies principles of classical frequency mixing to a

quantum system [23]. Classical frequency mixers shift signals to a different frequency range; they multiply two input signals such that the output is at a desired frequency. For example, a diode's non-linear relationship between voltage and current allows two input sinusoidal signals to be multiplied together, which by trigonometric properties results in new frequencies that are the sum and difference of the input frequencies [24]. This is used in quantum engineering to up-convert MW control fields to a desired frequency, usually the resonance of the quantum system. Quantum frequency mixing is a technique that uses the quantum system itself as the mixer, where the two input signals are multiplied by the intrinsic non-linearity in the dynamics of the quantum system. This is practically important in that it allows mixing on the nanoscale, offering resolution unavailable with classical mixers.

When the system is driven with two fields at different frequencies, the dynamics can be described as a quantum frequency mixer, where the effective Hamiltonian derived in the multi-mode Floquet picture provides an elegant approach as developed by Wang, *et al.* [23]. Here, we briefly reintroduce the principle of quantum frequency mixing and its application in this work. To bring a signal of frequency ω_s to resonance with a transition in an NV center, we apply a bias oscillating field with a frequency ω_b. Here, ω_s and ω_b are analogous to the input radio frequency and local oscillator of a classical mixer. The effective quantum signal generated by the nonlinear process, is at frequency ω_T, which is analogous to the intermediate frequency of a classical mixer as shown in Fig. 2-3.

Because this is a quantum system under a time-dependent drive, Floquet theory is required to predict the precise resonance frequencies and dynamics. In the Hilbert space, the combined effect of two Fourier components $H_b e^{i\omega_b t}$ and $H_s e^{i\omega_s t}$ caused by the combination of the input signal ω_s and the bias ac field ω_b are equivalent to an effective Hamiltonian with a frequency $\omega_b - \omega_s$. The effective target signal is thus a signal down-converted to the GHz resonance frequency of the NV system, and existing quantum sensing protocols such as the Rabi magnetometry sequence described in Sec. 2.3 can be used to probe the system.

Wang, *et al.* describes multiple pulse sequences for quantum frequency mixing.

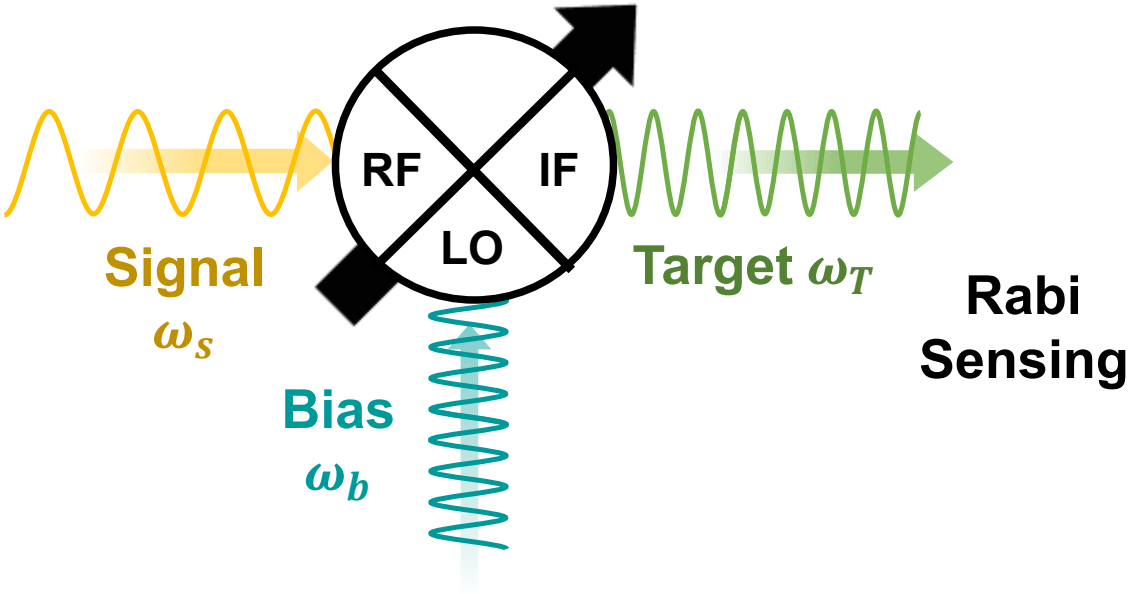

Figure 2-3: Visual of quantum frequency mixing for Rabi sensing. In the presence of a signal field (yellow) at ω_s, which is analogous to the RF signal of a classical mixer, and a control or bias field (teal) at ω_b, which is analogous to a classical local oscillator, a target field (green) at the sum or difference frequency ω_T is generated, which matches the resonance of the NV system.

We implement a quantum frequency mixing scheme to detect a signal oscillating in the plane of the NV axis using a Rabi pulse sequence. The Hamiltonian for such a scheme in the lab frame for a signal with frequency ω_s is given as:

$$H = \frac{\omega_0}{2}\sigma_z + \Omega_{sz}\cos\left(\omega_s t + \phi_s\right)\sigma_z + \Omega_b\cos\left(\omega_b t + \phi_b\right)\sigma_x \tag{2.18}$$

where Ω_b is the amplitude of the bias field, Ω_{sz} is the amplitude of the signal frequency projected along the z-axis, and ϕ_b, ϕ_s are the phases of the bias and signal respectively. Using the same interaction picture as for a normal Rabi sequence: $U_0 = e^{i(\omega_0 t/2)\sigma_z}$ and applying multi-mode Floquet theory to solve for the mixed frequency effective Hamiltonian gives:

$$
\begin{aligned}
H_I = \frac{\delta_z}{2}\sigma_z + \Omega_{Tz}\cos\left[\left(\omega_b - \omega_0 - \omega_s\right)t + \left(\phi_b - \phi_s\right)\right]\sigma_x \\
+ \sin\left[\left(\omega_b - \omega_0 - \omega_s\right)t + \left(\phi_b - \phi_s\right)\right]\sigma_y \\
-\Omega'_{Tz}\cos\left(\left(\omega_b - \omega_0 + \omega_s\right)t + \left(\phi_b + \phi_s\right)\right)\sigma_x \\
+ \sin\left[\left(\omega_b - \omega_0 + \omega_s\right)t + \left(\phi_b + \phi_s\right)\right]\sigma_y
\end{aligned} \tag{2.19}
$$

where the amplitude of the target signal field at $\omega_b - \omega_0 - \omega_s$ projected along the z-axis, is given by

$$
\Omega_{Tz} = \frac{\Omega_{sz}\Omega_b}{4}\left(\frac{1}{\omega_b - \omega_0} + \frac{1}{\omega_s}\right) \tag{2.20}
$$

[23]. Wang, *et al.* makes the following assumptions for the first order Floquet theory approximation to work for this sequence: $\Omega_{sz}, \Omega_b, |\omega_b - \omega_0 \pm \omega_s| \ll \omega_s$. We choose a bias frequency ω_b such that:

$$
\omega_b - \omega_0 - \omega_s = \delta_z \tag{2.21}
$$

where δ_z is the detuning from the frequency-mixed resonance. Using the classical mixing analogy, this essentially says:

$$
\omega_b - \omega_s = \omega_T = \omega_0 \tag{2.22}
$$

with ω_0 the NV resonance frequency. This makes an effective Hamiltonian similar to Eq. 2.5 that induces Rabi oscillations. The oscillation frequency experimentally measured when using this protocol is proportional to the inverse of the signal frequency

$$\Omega_{\mathrm{QFM}} = \frac{\Omega_{sz}\Omega_b}{\omega_s}. \tag{2.23}$$

where $\Omega_{\mathrm{QFM}} = 2\Omega_{Tz}$. With this frequency, we can extract the amplitude of the signal. The full details of the multi-mode Floquet theory and the derivations for this quantum frequency method are found in Wang, *et al.* [23].

Chapter 3

Wide-field Magnetic Imaging

3.1 Nitrogen-Vacancy Magnetic Imager Concept

NV centers can be used for high-spatial-resolution, wide-field-of-view imaging of microscopic magnetic fields. A diamond magnetic imager is a type of bulk ensemble sensor; it employs a large number of NV centers and statistically averages the results to determine the magnetic field strength. This yields a higher signal-to-noise ratio than an individual NV center; however, ensembles have more complicated spin bath environments that can speed up decoherence and dephasing [5, 8, 20]. Diamonds with bulk ensembles of NV centers can have NV centers oriented along all four crystallographic directions. If we apply the static magnetic field along a specific NV axis direction, we can selectively address that NV orientation subset, which becomes our z direction.

Figure 3-1 shows a schematic of an NV diamond magnetic imager. At the top is a macroscopic, single-crystal diamond chip with a thin, uniform layer containing a high concentration of NV centers at the surface. A laser excites NV centers in a region of the diamond chip, causing the NV centers to emit fluorescence, which can yield spatially-resolved magnetic field information by imaging the light onto a sensor array using a set of imaging optics. We place a test structure with a spatially-varying magnetic field on top of the diamond. As described previously in Chap. 2, the amount of fluorescence emitted by the NV centers depends on the magnetic field

strength of the signal being sensed. Thus, for a spatially-varying magnetic field, the sensor array will map out the spatially-varying fluorescence from the different sections of NV centers, thereby creating a "magnetic" image. Because the NV centers across the chip fluoresce simultaneously, these imagers have faster image acquisition times than other imaging techniques like raster scanners. This speedup of acquisition time adds spatio-temporal dynamics to the traditional imaging techniques, since images can be taken in rapid succession [5, 22].

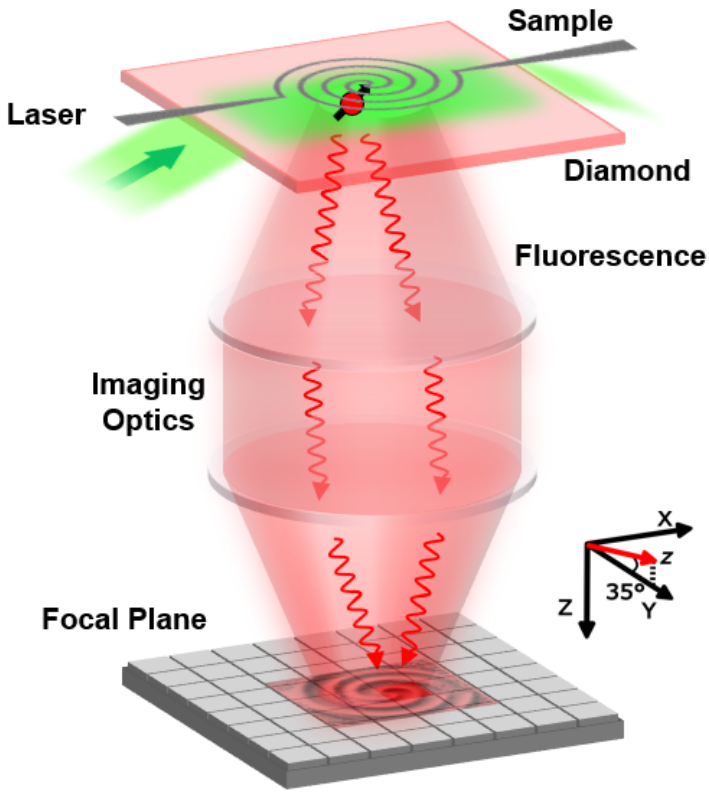

Figure 3-1: Schematic diagram of an NV diamond magnetic imager. A green laser illuminates a region of NV centers in diamond. A specific region of the diamond sensor film (highlighted by a red cartoon spin) responds to the magnetic field in that region and produces magnetic-field-dependent fluorescence, which is imaged onto a sensor array using a set of imaging optics. An example test structure generating a spatially-varying magnetic field, a spiral with attached wire leads, is displayed at the sensor plane, and an image of the magnetic field-dependent NV fluorescence due to the test structure is projected at the focal plane.

3.2 Experimental Methods for Imaging

Figure 3-1 also shows the relevant coordinate systems we use to orient our experimental setup: $\{x, y, z\}$ indicates the NV coordinate system (with z along the N-V axis we selectively address, which is also the diamond [111] crystallographic axis) and $\{X, Y, Z\}$ indicates the imager coordinate system (with Z out of plane for the image). For our magnetic imager, a $5 \times 5 \times 0.5$ mm^3 diamond sample with a 20 µm layer of NV centers is illuminated with 1 W of 532 nm laser light, which is passed through an acousto-optic modulator (AOM) switch and flat-top beam shaper. We place the test structures on top of the NV center layer, which is coated with 10 nm of Ti metal and then 50 nm of Au to prevent light leakage. The diamond is attached to a mount that applies a uniform microwave field along the x direction, and the NV centers detect DC magnetic fields (with Ramsey magnetometry) and AC magnetic fields (with QFM) along the z-axis. The mount also acts as a heat sink to dissipate diamond laser heating. We applied a 1 mT bias magnetic field B_0 along the $+z$ direction using permanent magnets. This bias field sets the transition frequencies between NV ground-state sublevels to be $D \pm \gamma B_0$, where $D \approx 2870$ MHz is the zero-field splitting, and we use $\omega_0 \sim 2890$ MHz (the resonance fluctuates with temperature by -74.2 kHz/K [25, 26]). NV fluorescence light is imaged with an optical microscope onto a digital focal-plane array (DFPA) camera, which allows for the combination of high sensitivity, large dynamic range, large pixel count, on-chip processing, and fast data rates required for this work [27]. The laser, microwaves, test structure current, and camera trigger pulses are programmed with a 1.2 GS/s arbitrary waveform generator (AWG), see Appendix B.4 for details. The camera is triggered to acquire an NV fluorescence readout image, which is converted to a magnetic field image.

3.3 Experimental Ramsey Pulse Sequence

We first demonstrate our imaging capabilities for sensing static magnetic fields. We apply a DC current to the test structure and perform Ramsey magnetometry. This

helps us validate our AC imaging technique by ensuring that the test structure is centered in the camera field of view and confirming that the test structure is flat on the diamond surface. It also provides us with a DC magnetic image to compare with subsequent AC QFM magnetic images.

For our Ramsey measurements, we used slope detection to convert the measured phase into magnetic field as shown in Fig. 3-2. At the point of maximum slope, a sinusoid is approximately linear. In this range, a change in fluorescence can be mapped linearly to a change in phase and consequently magnetic field. Using slope detection enables us to achieve higher sensitivity with our sensor; however, the dynamic range (the range of magnetic field amplitudes that can be detected) when using slope detection is limited by phase wrapping. If the signal is strong enough to accumulate phase greater than a $\pi/2$ period of the oscillation, then it will be outside this linear region [1].

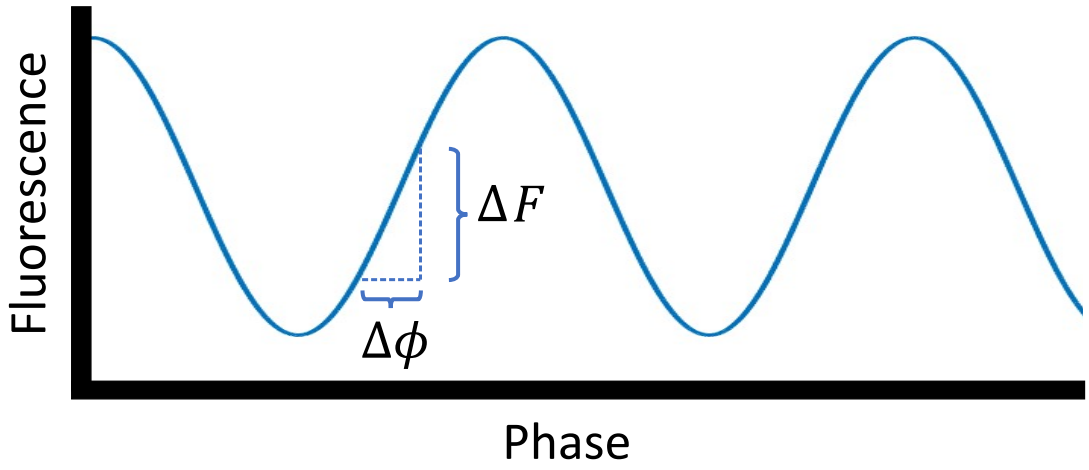

Figure 3-2: Visual demonstration of linear detection. At the point of maximum slope, the change in fluorescence is approximately linear to the change in phase, so collecting the change in fluorescence in this region can be mapped to a change in phase, which can be converted to magnetic field values.

From Eq. 2.15, the accumulated phase is proportional to both the magnetic field to be sensed and the precession time τ_{Ramsey}, which means that increasing the precession time increases the sensitivity of magnetic fields that can be measured. However, this must be balanced with the dephasing time $T_2{}^*$, which is caused by inhomogeneities across the ensemble of NV centers (i.e. variations in the local spin environment). The

optimal time for a measurement τ_{Ramsey} is when the fluorescence has decayed to 1/e of its initial value [20].

Figure 3-3 depicts the experimental steps we used to perform a DC magnetometry experiment. We first start by performing a conventional Rabi magnetometry measurement. To do this, we initialize the NV centers to the $m_s = 0$ magnetic sub-level with a laser pulse, apply a uniform MW field across the diamond with our estimate of ω_0 for a variable duration τ_{Rabi}, and read out the NV final state with a second laser pulse. The camera exposes for the length of the readout pulse. Fitting the NV fluorescence intensity as a function of τ_{Rabi} for each pixel and sweeping the MW frequency until we have the largest contrast and slowest Rabi frequency on average over the field of view ensures we are on-resonance (from Eq. 2.9). The Rabi frequency also determines how long to turn on the MW drive field to create a $\pi/2$ pulse, i.e. satisfy $\Omega\tau_{\text{Rabi}} = \pi/2$.

We then perform a precession time sweep as shown in Fig 3-3a. A precession time sweep involves successive pulse sequences where we fix the start of one $\pi/2$ pulse and vary the start of the other $\pi/2$ pulse, sweeping the length of the precession time τ_{Ramsey}. Mapping the Ramsey Free Induction Decay allows us to find the dephasing time T_2*. We then perform a phase sweep, where we fix the precession time τ_{Ramsey} as shown in Fig. 3-3b. Using digital phase shifters, we fix the phase of one microwave pulse and perform successive measurements where we sweep the phase of the other microwave pulse. This acts as an artificial magnetic field applied equally across the entire diamond, allowing us to see how the fluorescence changes with each phase for each pixel. This is important for wide-field imaging, since inhomogeneities across the diamond cause the NV centers in each region to precess slightly differently, so performing this phase sweep allows us to know how each region changes in response to a magnetic field. We save this information as a matrix containing the slope and intercept values for each pixel to map change in fluorescence to a change in the magnetic field. Finally, we perform a magnetometry sequence as shown in fig 3-3c. We fix both the free precession time τ_{Ramsey} and the phase ϕ of the first and second microwave pulses so that for as many pixels as possible are within the linear regime.

In a simplified version, we perform two sequences. In the first sequence, we apply a signal current to the device under test, creating a magnetic field to be sensed, and a second where the signal current is turned off. We subtract the fluorescence collected during the "off" sequence from the "on" sequence to determine the difference in fluorescence caused by the signal magnetic field. We then apply the calibration matrix to convert the change in fluorescence to a change in phase, which we can convert to a magnetic field value. In practice, we apply a noise subtraction protocol where we modulate the signal amplitude with positive/negative DC current between alternate camera exposures to improve the long-term stability and pixel-to-pixel noise floor of our apparatus. For details, see Appendix A.1. We also implement the double quantum four-Ramsey protocol, which involves applying two microwave frequencies to address both the $m_s = +1$ and $m_s = -1$ levels at the same time to avoid frequency shifts due to temperature and strain inhomogeneity, as well as a sequence subtraction protocol to cancel out residual single-quantum coherence from pulse imperfections [28]. The double quantum technique is described at length in [28, 29].

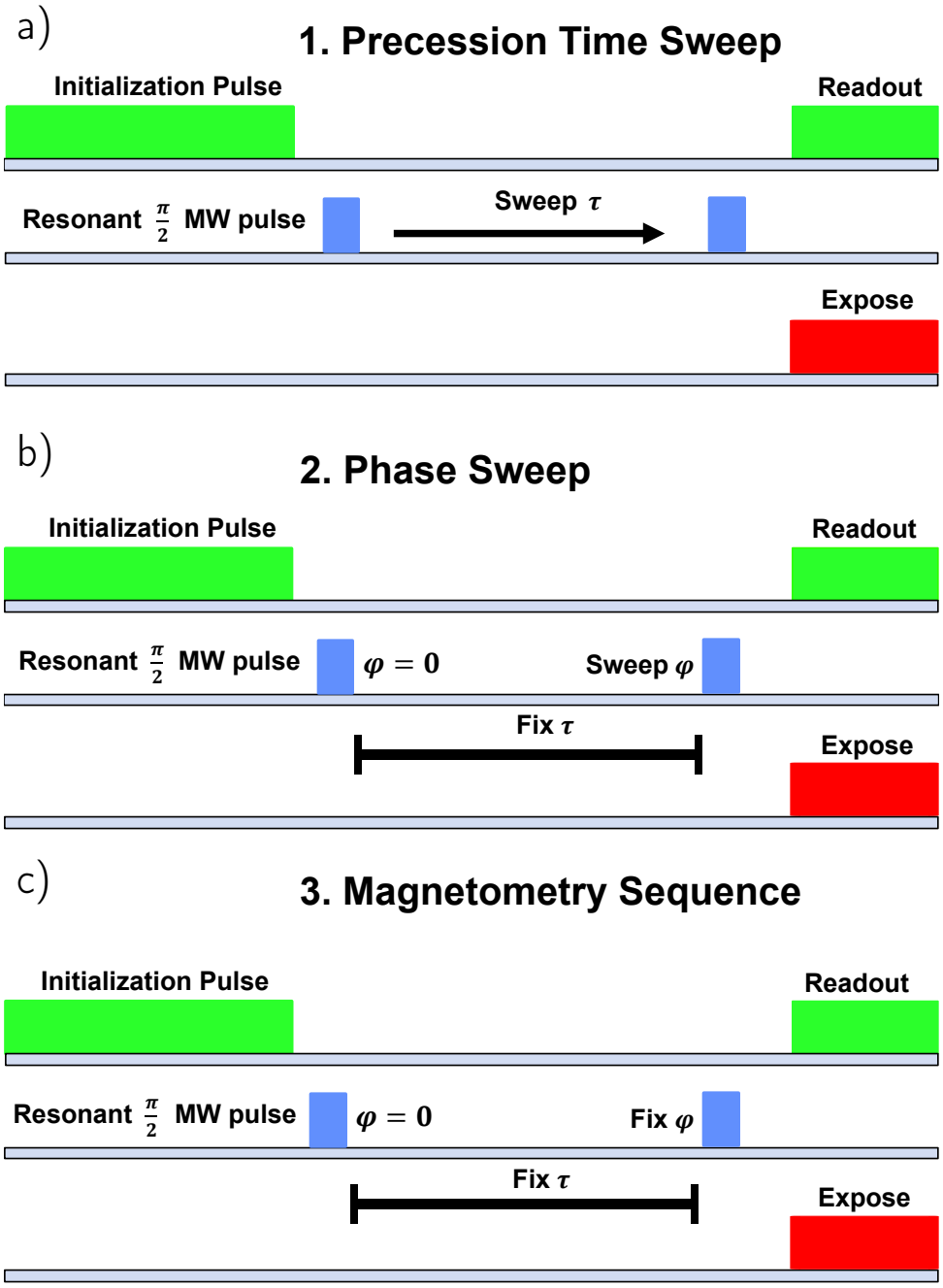

Figure 3-3: Pulse Sequence steps for a Ramsey magnetometry experiment. (a) The first step is a series of successive pulse sequences that sweeps the duration of the free precession time τ_{Ramsey}. (b) The second step is a series of successive pulse sequences where τ_{Ramsey} is fixed, but the phase of the second MW pulse is swept. This gives the calibration matrix to convert fluorescence to magnetic field. (c) The last step is the magnetometry sequence, where τ_{Ramsey} and ϕ are fixed on a point of maximum slope (see 3-2). At least two sequences are performed, one where the signal to be detected is on and one where it is off. The difference in fluorescence can then be converted using the calibration matrix for each pixel to find the magnetic field value at a given point.

3.4 Through-Silicon Via Test Chip at DC

We performed imaging on an integrated circuit fabricated in the microelectronics facility at MIT Lincoln Laboratory. We achieved <20 μm spatial resolution over an approximately 1.5 $\times$ 1.5 mm^2 field of view. The integrated circuit originally was designed and fabricated to test a 3D integration technique for scaling up superconducting technology, whereby an interposer tier containing through-silicon vias (TSVs) connects a pristine high-fidelity qubit layer to a layer designated for signal routing and control. The test chip contains arrays conducting traces in separated layers bridged by TSVs, all daisy-chained in series so that current flows from one end of the chip to the other through higher and lower layers and also across alternating rows (see Fig. 3-4).

The test chip is placed in close proximity to the diamond surface. We apply a 5 V DC signal across the measured $\approx$ 17 kΩ resistance. Figure 3-5 shows the magnetic field projection along the z-axis. Due to a calibration error, the values are in approximate magnetic field units within a factor of two of μT. The image clearly shows the structure expected from the daisy-chained chip. The image has regions of higher field magnitude separated by regions of lower field magnitude. The spacing between these regions is consistent with the spacing between regions with conductive traces residing in shallow and deeper layers. Moreover, the sign of the field is consistent with the alternating current direction in adjacent rows and the pattern is consistent with the known row spacing.

We also used the TSV structure to demonstrate the temporal dynamics of the magnetic imager. Figure 3-6 shows a frame from a magnetic movie showing the field created by the TSV chip change over a 0.3 s time period. We sent a signal current through the TSV chip that varies temporally as a heart-beat signal. The magnetic field strength changes over time and spikes with each beat at these two locations on the chip. 3-6b shows the initial signal current through the chip as a function of time. 3-6c-d show the average magnetic field value of the pixels in the upper and lower box respectively as a function of time. Since the current is going in opposite directions at

those points, they have opposite positive and negative values.

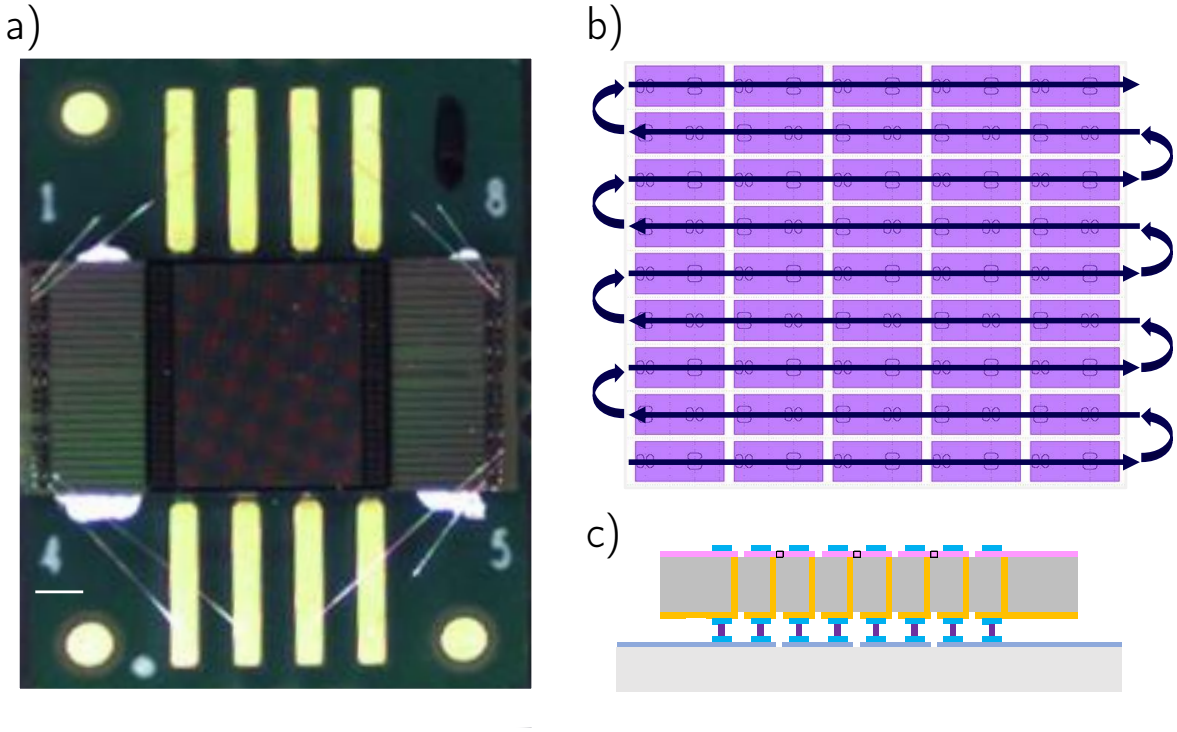

Figure 3-4: (a) Optical image of through-silicon via (TSV) test chip. White scale bar in the bottom left denotes 1 mm. (b) Diagram depicting the daisy-chained TSV test structure. Arrows show the current path though adjacent rows, traveling in alternating directions. The purple rectangles refer to conductive traces, which are spaced by 100 μm in the vertical direction and 200 μm horizontally. The small ovals represent TSVs through which current can flow to a deeper layer, which has conductive traces spanning the insulating gaps shown in the layer displayed. (c) Schematic depicting a side view of a single row of the TSV chip. The colored regions conduct current while the gray regions are insulating. Current must flow between the higher and lower layers in order to travel from one side of the row to the other.

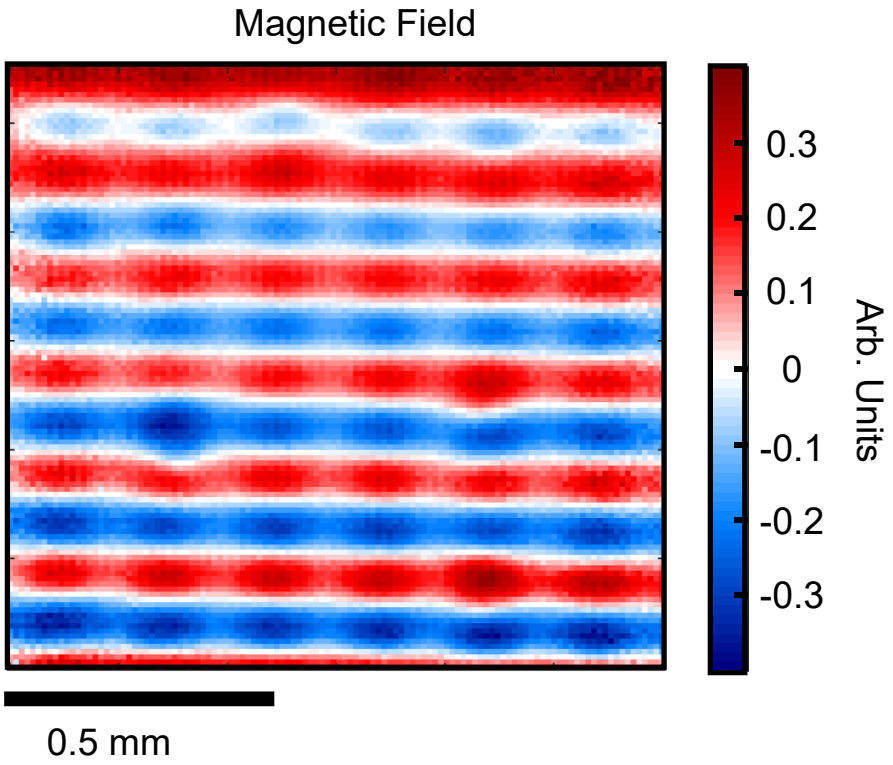

Figure 3-5: Magnetic field image of the through-silicon via test structure measured along the z-axis. The image shows regions of higher magnetic field values and lower magnetic field values corresponding to the movement of the trace in and out of the plane. As the current moves back and forth across the chip, the magnetic field values alternate from positive to negative. The values are in approximate magnetic field units within a factor of two of μT.

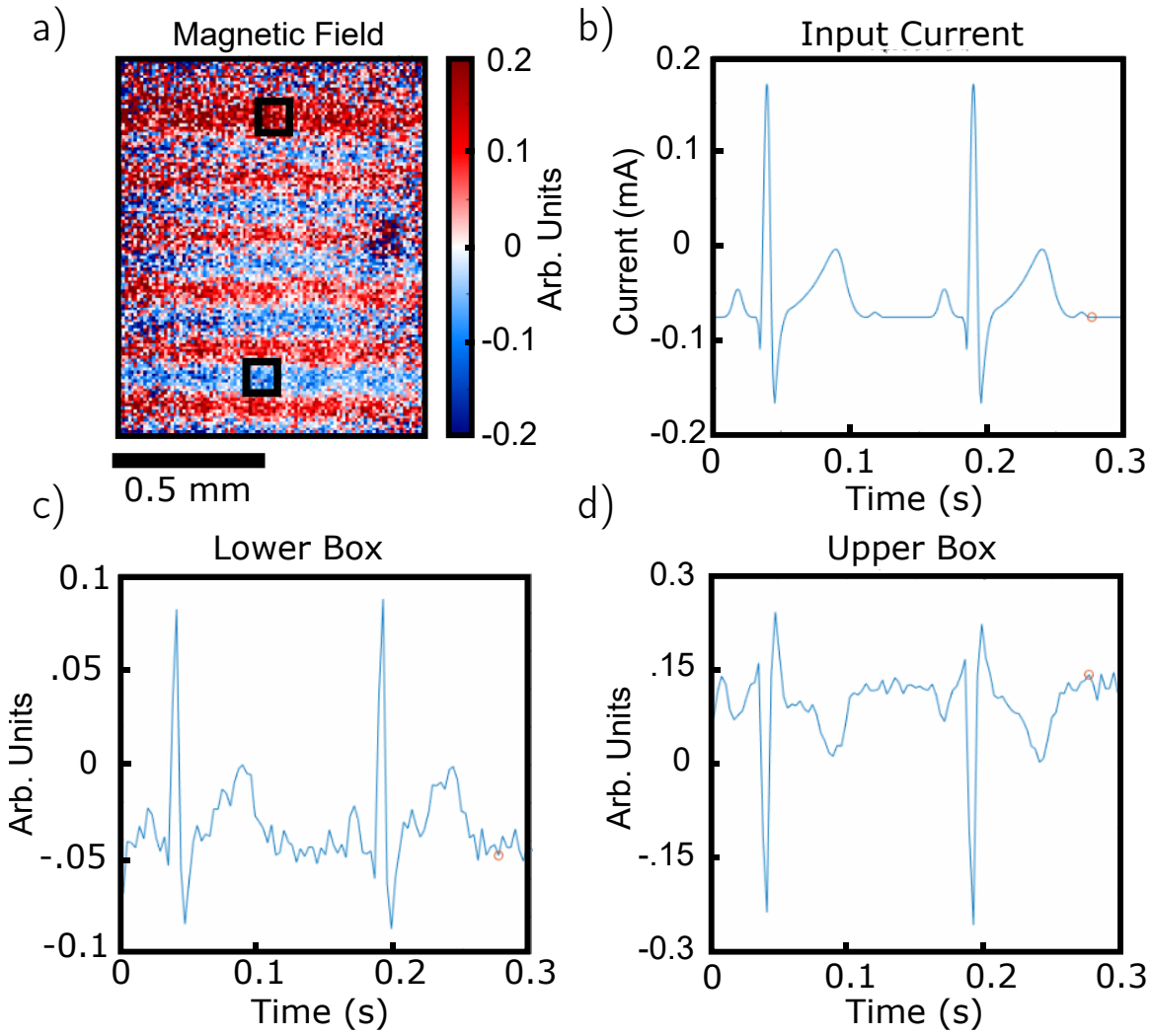

Figure 3-6: Screen shot of magnetic movie (a) A magnetic image near the end of the movie. (b) the amplitude of the signal current at each point in time, creating a heartbeat waveform. The circle shows the current applied to the signal in the magnetic image in a. (c) The measured magnetic field value average of the lower box of pixels. (d) The measured magnetic field value average of the upper box of pixels. Since the upper and lower boxes are in regions where the current is going in opposite directions, the magnetic field value has opposing positive and negative signs in these boxes.

Chapter 4

Quantum Frequency Mixing on an Imager

4.1 Experimental Quantum Frequency Mixing Pulse Sequence

To experimentally execute a Rabi-based QFM pulse sequence, we once again start with a conventional Rabi sequence by applying a uniform MW field across the diamond to find the resonance with no signal applied to the test structure. This provides the resonant ω_0 frequency needed to find the correct frequency for ω_b. The on-resonance Rabi frequencies also provide the amplitude Ω_b needed to convert the detected Rabi frequencies Ω_{QFM} to a magnetic field value.

We then apply an AC current with frequency ω_s and increase the uniform MW field frequency to $\omega_b = \omega_0 + \omega_s$ and measure the resulting QFM Rabi oscillations. Figure 4-1 visually demonstrates the full QFM protocol on an imager. The QFM experiment is nearly identical to the on-resonance Rabi oscillation experiment, with the main difference being that we address the NV centers with frequency ω_b instead of ω_0. Fitting the fluorescence time-trace data to extract Ω_{QFM}, we can then use Eq. 2.23 to extract the AC signal field amplitude for each pixel. Figure 4-2 provides a summary comparing all of the different pulse sequences used to implement and

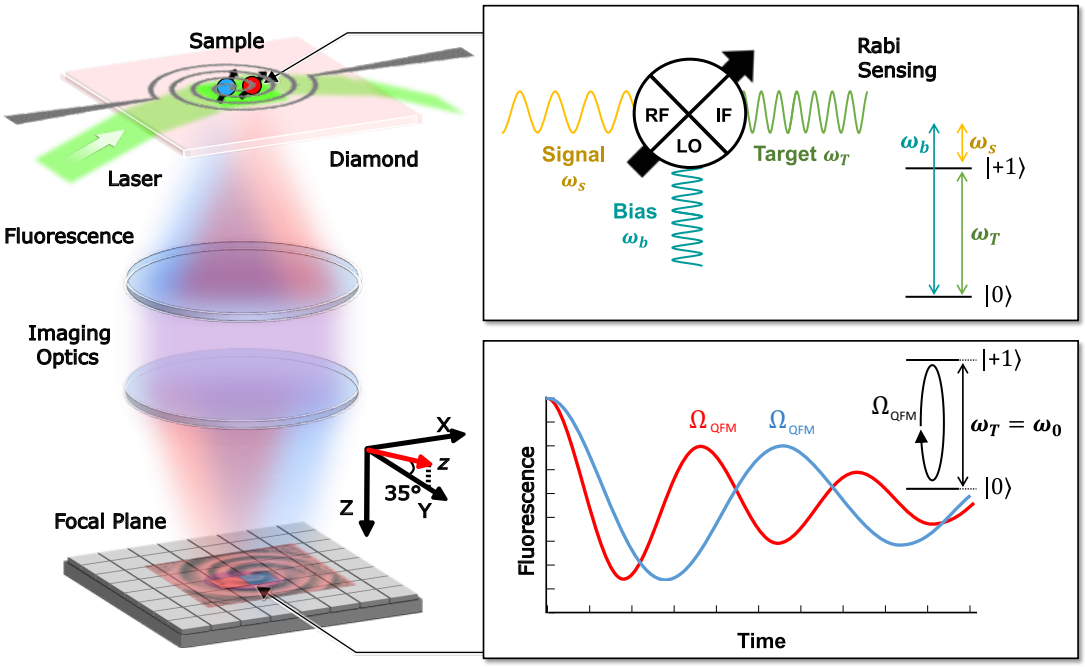

Figure 4-1: (a) Schematic diagram of QFM on a magnetic imager. Different regions of the diamond sensor film (highlighted by blue and red cartoon spins) respond to spatially-varying magnetic fields and produce magnetic-field-dependent fluorescence, which is imaged onto a sensor array using a set of imaging optics. (b) The spins act as both quantum mixers and quantum sensors. In the presence of a signal field (yellow) at ω_s and a control or bias field (teal) at ω_b, a target field (green) at the sum or difference frequency ω_T is generated. (b) When ω_b is chosen so that the field at the sum or difference frequency is resonant with the spin transition at ω_0, population oscillations occur between the two spin states. The frequency of oscillations, called the QFM Rabi frequency Ω_{QFM}, provides a measure of the amplitude of the signal field, for a known bias field amplitude, given by Eq. 2.23. Spatial variations in field amplitude result in variations in Ω_{QFM} at arbitrary ω_s.

validate the QFM technique for magnetic imaging.

As with the DC images, we modulate the signal, turning it on and off and subtracting alternate frames to improve the long-term stability and pixel-to-pixel noise floor. See Appendix A.1.

4.2 Test Structures

To demonstrate the QFM technique on our imager, we fabricated two conducting test structures on a glass microscope slide using photolithography and electron-beam

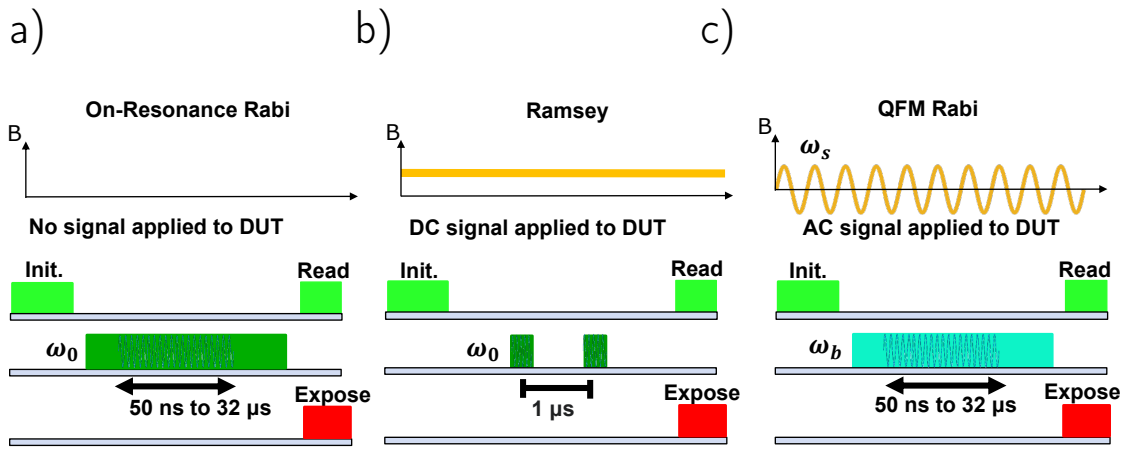

Figure 4-2: (a) Conventional Rabi pulse sequence used to determine the resonance of the diamond. No current is applied to the device under test (DUT). We initialize the NV centers to the $m_s = 0$ state with an optical laser pulse, apply an on-resonance microwave field of frequency ω_0 for a variable duration and read out the state with a final laser pulse. (b) Ramsey pulse sequence. We apply a DC signal to the DUT. Instead of varying the duration of the on-resonance pulse, we apply a $\pi/2$ microwave pulse to create a superposition of the $m_s = 0, m_s = 1$ states and allow the system to evolve for a fixed time τ_{Ramsey}. We then apply another $\pi/2$ pulse, followed by an optical pulse to read out the state. (c) Quantum frequency mixed (QFM) Rabi pulse sequence used to measure an AC magnetic field. We apply a signal current with frequency ω_s to the DUT. We then apply an adapted Rabi sequence where instead of resonant MW pulses, we apply MW pulse sequences with bias frequency ω_b. We then read out the state with a final optical pulse.

evaporation (10 nm Ti, 2 µm Al, 10 nm Ti, 150 nm Pt, 200 nm Au), a straight wire and an Archimedes spiral (both with 50 µm trace thickness), as shown in Fig. 4-3a and Fig. 5-1a. The space between turns for the Archimedes spiral is 200 µm. We attached wire leads to the test structures using silver paint (yielding few-Ω total resistances), after which they were placed on the diamond sample. When applying DC and AC currents using a function generator, we included a 50 Ω load resistor in series and measured the voltage across across it to validate the DC and AC current amplitudes through the test structures.

4.3 Results

4.3.1 Initial Validation

Figure 4-3a shows a photo of the straight wire structure we imaged. We applied an 80 mA peak-amplitude AC current through this structure and measured the projection of the created magnetic field along the z-axis. The acquisition times for each images was ∼5 minutes, ∼2 minutes of which was dead time due to camera transfer lag. The Rabi frequency is extracted from the time-averaged Rabi oscillations using the fit function $C(\tau_{\text{Rabi}}) = A\cos\left(\Omega_{\text{QFM}}\tau_{\text{Rabi}} + \phi\right)e^{-\tau_{\text{Rabi}}/T} + f$ where C is the fluorescence intensity, A is the Rabi amplitude, ϕ is a phase offset, T is the Rabi lifetime, and f is an offset. See Appendix A.1 for details on the acquisition times and the normalized fluorescence intensity. Figure 4-3b maps the Ω_{QFM} values for $\omega_s = 2\pi\times4$ MHz and $2\pi\times35$ MHz, including the Rabi oscillations for an example pixel. As expected, at higher signal frequencies, the detected Rabi frequency decreases. There is a black stripe that corresponds to a Rabi frequency near 0, which matches where the field is perpendicular to the z direction.

Figure 4-3d plots Ω_{QFM} as a function of ω_s for two pixels. As expected, Ω_{QFM} decreases as ω_s increases. These data are fitted with the fit function $\Omega_{\text{QFM}} = a/\omega_s$ (where a is a free parameter), and are consistent with Eq. 2.23. For both pixels, Ω_b was experimentally determined to be $\sim 2\pi\times1.0$ MHz. Ω_{sz} is roughly estimated to be $\sim 2\pi\times2$ MHz and $\sim 2\pi\times4$ MHz for the center and right pixels respectively, based on the simulated magnetic field of a 50 μm ribbon at ∼50 μm standoff distance. The fitted a coefficients are $(2\pi)^2 \times \{1.3, 2.3\}$ MHz^2 for the center and right pixels. Given $\Omega_b \sim 2\pi\times1.0$ MHz for both pixels and the simulated Ω_{sz} are $\sim 2\pi \times \{2, 4\}$ MHz, the extracted fit parameters are within a factor of two of the estimated values and are thus reasonably consistent with the Floquet theory prediction.

Previously, quantum frequency mixing was demonstrated for a bulk NV ensemble (equivalent to a single-pixel measurement). The above straight-wire demonstration shows that this technique works for an NV imager, confirming the anticipated frequency-scaling law.

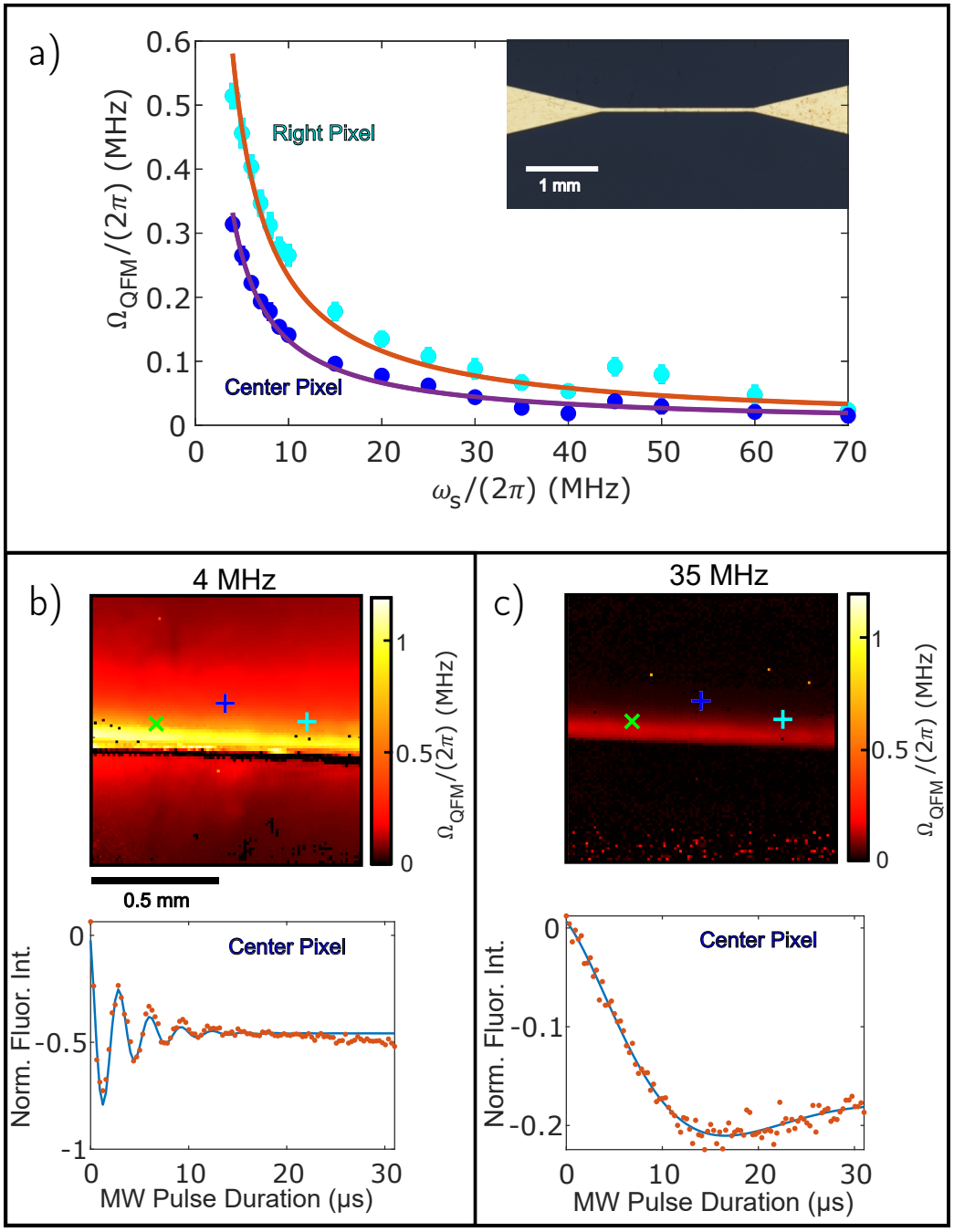

Figure 4-3: (a) Rabi frequencies Ω_{QFM} for the center and right pixels in the magnetic images shown in b-c at different input signal frequencies ω_s fit to an a/ω_s curve, demonstrating their inverse relationship as described in Eq. 2.23. A photo of the straight wire structure is shown in the upper corner. (b-c) Two example images demonstrating quantum frequency mixing for an AC current through a straight wire at $\omega_s = 2\pi\times4$ MHz and $2\pi\times35$ MHz respectively. The Rabi oscillations and the extracted Rabi frequency for the specified center pixel are shown below the images. As expected, the detected Rabi frequency Ω_{QFM} at a specified pixel decreases at higher input signal frequencies ω_s. The green pixel will be discussed in Sec. 4.3.3.

4.3.2 Strong-Drive, Low Signal Frequency Regimes

In Fig. 4-3 we used Eq. 2.23 to confirm that the measured QFM Rabi frequencies Ω_{QFM} were behaving as expected. However, this expression is validated by the Floquet theory prediction when

$$\Omega_b,\ \Omega_{sz} \ll \omega_s, \tag{4.1}$$

which is not necessarily true for all experimental conditions.

Figure 4-4a shows the Ω_{QFM} vs. ω_s behavior for the pixel on the left in the straight wire validation image, marked with a green $\times$ symbol, which has a stronger amplitude Ω_{sz}. Here, the value for Ω_b is $2\pi\times1.0$ MHz, Ω_{sz} is $\sim 2\pi\times2.5$ MHz, and the lowest value for ω_s is $2\pi\times2$ MHz. As ω_s decreases towards Ω_{sz}, Ω_{QFM} reaches a maximum around $\omega_s = 2\pi\times5$ MHz and then decreases, violating Eq. 2.23. We estimate Ω_{sz} for this pixel by excluding the lower ω_s values where the assumptions are violated and fitting the higher values to the a/ω_s curve to extract Ω_{sz}. To confirm this behavior, we perform a computational simulation of the experiment by inputting the laboratory frame Hamiltonian and the time evolution operator and numerically solving for the population over a discrete set of time points, then taking a Fourier transform of the population oscillations to find the effective Rabi frequency. As we plot the effective Rabi frequency across different input signal frequencies, we see that this behavior is accurately reproduced. Note that Ω_b was extracted using an on-resonance Rabi measurement, and Ω_{sz} was extracted by fitting the high-frequency tail of the measurements in Fig. 4-4a (where the assumption is valid). Figure 4-4b shows the simulation for the center pixel, demonstrating that both the simulation and experimental data shown in 4-3 match Eq. 2.23.

In order to determine where the Floquet theory prediction breaks down, we repeated the experiment and simulation, this time fixing the signal frequency at $\omega_s = 2\pi\times5$ MHz and calculating the effective Rabi frequencies for the center pixel in Fig. 4-3 across different amplitudes of the signal Ω_{sz} as demonstrated in Fig. 4-5. The experimental data and the simulation match the Floquet theory prediction reasonably well at lower values of Ω_{sz} but veer away significantly as Ω_{sz} approaches

ω_s.

This analysis shows a potential weakness of the QFM AC magnetometry and imaging method, which is that the conversion from Ω_{QFM} to Ω_{sz} (which is nominally straightforward if using Eq. 2.23) may be nontrivial if Eq. 4.1 is invalid. This may complicate the QFM AC magnetometry method when attempting to apply it to more general experimental situations. For example, one may be tempted to increase Ω_b to compensate for a small Ω_{sz} (implying a slow Ω_{QFM}, which could be difficult to measure if its period is slow compared to T_{Rabi}). However, such a strategy could violate Eq. 4.1, requiring more complicated calibration needed to extract Ω_{sz}.

4.3.3 Weak-Drive Regimes

In experimental conditions where Ω_{sz} is too small to extract a Rabi frequency Ω_{QFM}, one could apply an on-resonance $\pi/2$-pulse at frequency ω_0 before the Rabi pulse at frequency ω_b, making the NV fluorescence intensity proportional to $\sin\left(\Omega_{\mathrm{QFM}}\tau + \phi\right) e^{-\tau/T_{\mathrm{Rabi}}}$ instead of $\cos\left(\Omega_{\mathrm{QFM}}\tau + \phi\right) e^{-\tau/T_{\mathrm{Rabi}}}$ [14]. Similar to the slope detection scheme for the Ramsey sequence described in Sec. 3.3, for small Ω_{QFM}, the fluorescence change would be proportional to $\Omega_{\mathrm{QFM}}\tau$ for improved sensitivity and minimum-detectable Ω_{QFM}. However, implementing this also requires careful calibration to map the change in fluorescence back to a magnetic field value [1]. Note that if the phases between the initial $\pi/2$-pulse and the QFM pulse are uncontrolled, this may become more nontrivial to implement and interpret.

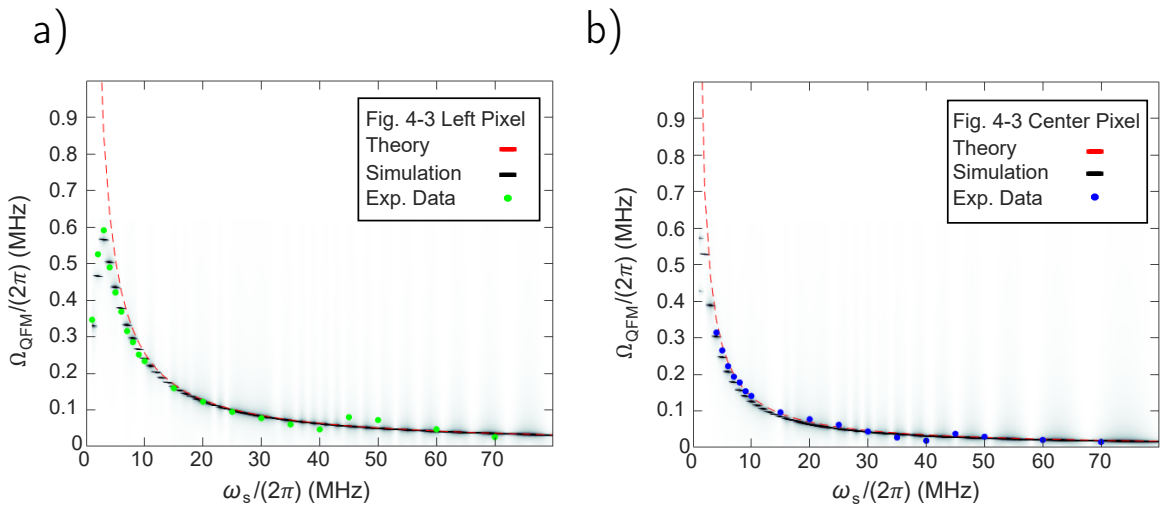

Figure 4-4: (a) Numerical simulation of Rabi frequencies Ω_{QFM} for the left (green) pixel in Fig. 4-3c-d at different signal frequencies ω_s. The red line represents Eq. 2.23, the dashed lines are the Fourier spectrum from the numerical simulation, and the green dots are the experimental data. At lower signal frequencies, the Floquet theory fails as Eq. 4.1 is violated, and Ω_{QFM} reaches a maximum before decreasing for both the simulation and experimental data. (b) The simulation comparison for the center pixel, which is plotted in Fig. 4-3d. For this pixel, the simulated data reasonably matches the Floquet prediction and experimental data, demonstrating that the assumptions hold for the Ω_b,Ω_{sz}, and ω_s values used in Fig 4-3.

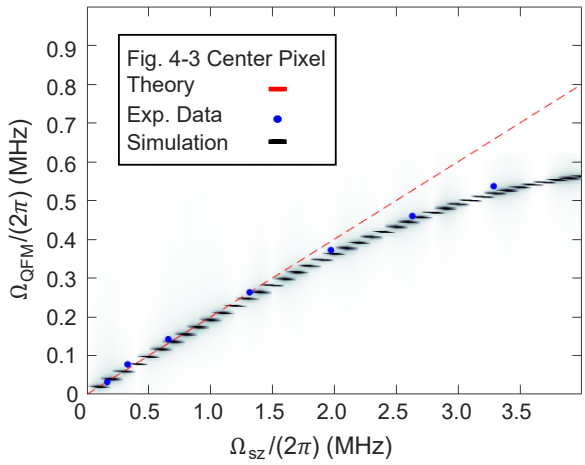

Figure 4-5: Numerical simulation of Rabi frequencies Ω_{QFM} for different signal amplitude values Ω_{sz} compared to experimental data and theoretical prediction Eq. 2.23 for the center pixel in Fig. 4-3c-d. This demonstrates where the Floquet theory fails as Ω_{sz} approaches ω_s and the assumption $\Omega_{sz} \ll \omega_s$ is broken.

Chapter 5

Imaging AC fields in Fabricated Devices

5.1 Archimedes Spiral Structure

In addition to a straight wire, we created a spiral structure using conductive materials on a glass microscope slide. We chose this test structure for its relative simplicity, allowing us to validate our results. However, unlike the simple straight wire structure, a spiral test structure has currents (magnetic fields) pointing in a wide range of directions, leading to a highly nontrivial magnetic field map. While not intended to be used as a planar spiral inductor, its layout is similar, and generalizing to measuring spiral inductors and other similar passive RF circuit elements is straightforward. Furthermore, since it is a passive circuit element, we have full control over the frequency and amplitude of current passing through the spiral. This is ideal for achieving a first proof-of-principle demonstration of QFM imaging. By contrast, when measuring the magnetic fields from a more sophisticated IC, these parameters are likely uncontrollable (and are often unknown).

Figure 5-1a shows a photo of the spiral structure. Figure 5-1b depicts the spiral structure with a 1 mA DC signal current measured using our Ramsey protocol. Figure 5-1c demonstrate the same spiral structure using the quantum frequency mixing technique. We once again applied an 80 mA peak-amplitude current through

this structure and measured the projection of the created magnetic field along the z axis. The images show the amplitude of the detected Rabi frequencies Ω_{QFM} at each pixel, with the Rabi oscillations at a specified pixel shown below. As expected, the Rabi frequencies for the pixel shown decrease by a factor $1/\omega_s$ as the input signal frequency increases from $\omega_s = 2\pi\times5$ MHz to $2\pi\times50$ MHz. Note that the DC image measures both positive and negative magnetic field values while the AC images measure amplitudes, though the absolute value of the DC image is consistent with the AC images.

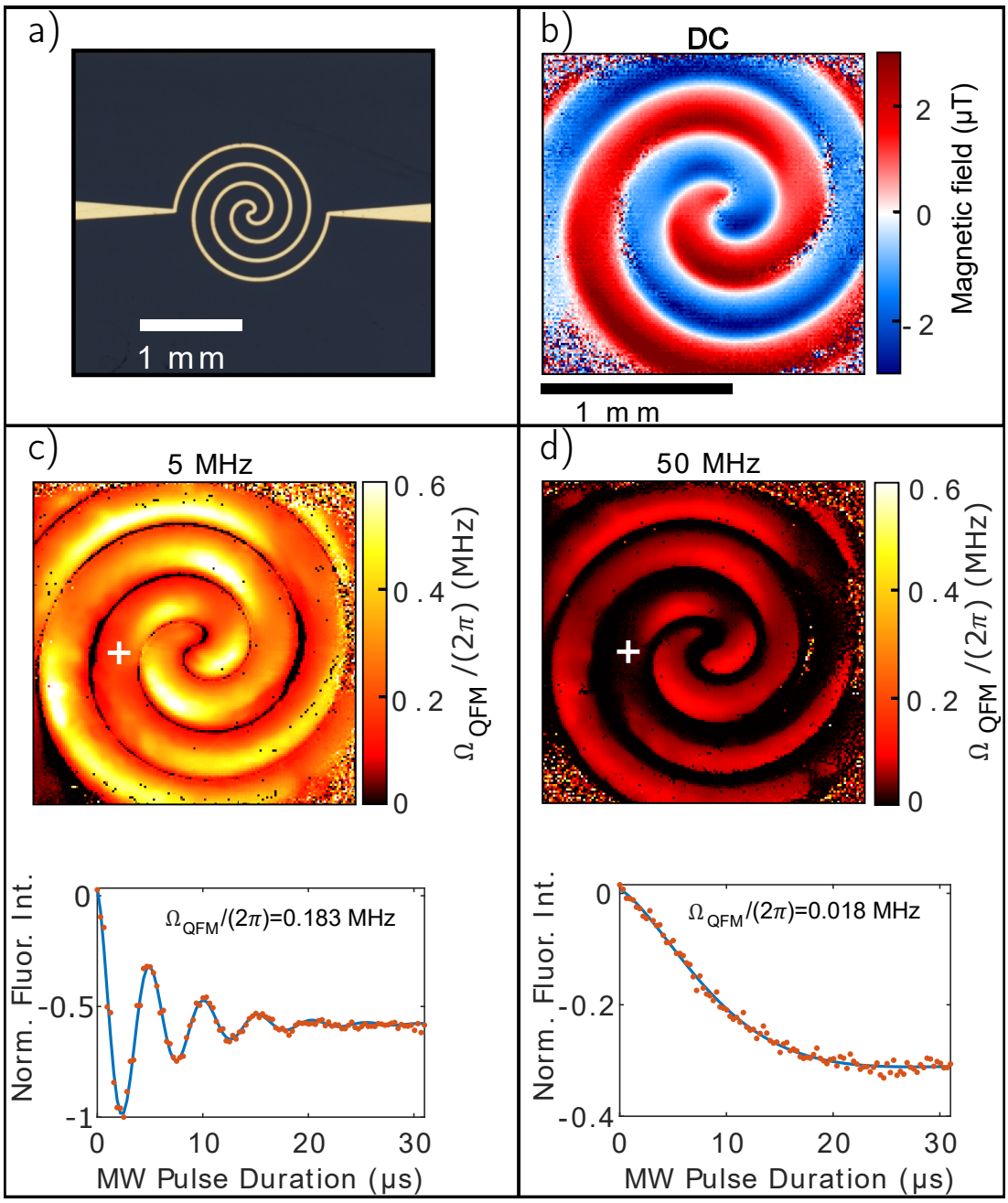

Figure 5-1: (a) Photo of the imaged spiral structure. (b) DC magnetic image of spiral structure with 1 mA signal current measured using a Ramsey sequence. (c-d) Two examples of AC magnetic imaging technique on a nontrivial spiral structure and the Rabi oscillations and extracted Rabi frequency for a specified pixel. The Rabi frequencies for a specified pixel decrease by a factor $1/\omega_s$ as the input signal frequency increases from 5 MHz to 50 MHz.

5.2 Through-Silicon Via Test Chip at AC Frequencies

We applied the QFM technique on the same TSV circuit chip described in Chapter 3 and measured the magnetic fields from the TSV structure after applying AC signal currents to it. Even at low AC input signal frequencies, we could not detect the same magnetic field structure as we could at DC fields. The structure we could see was even less discernible at higher frequencies. Figure 5-2b shows the absolute value of the magnetic field for a DC signal. In comparison, fig. 5-2c shows the detected Rabi frequencies when an $\omega_s = 2\pi\times1$ MHz AC signal is applied to the TSV structure. Figure 5-2d shows the Rabi oscillations for two different pixels.

We measured the impedance on a network analyzer and noted that it drops rapidly as the signal frequency increases, dropping from 17 kΩ at DC to an effective impedance of 2 kΩ at $\omega_s = 2\pi\times1$ MHz. We assume that the chip likely had some capacitive or inductive characteristic preventing us from seeing the structure, which we believe to be a capacitive short that caused the input signal to traverse a different path through the TSV chip. If the TSV image results are correct, this could enable us to discover the location of the capacitive short. Further analysis is needed to confirm that the chip's impedance is causing the change in what we detect as the AC magnetic signal, such as a simulation of the expected magnetic field at different frequencies. If the magnetic field matches the simulation, then this could demonstrate the potential to use quantum frequency magnetic imaging as a technique for characterizing impedance changes in devices.

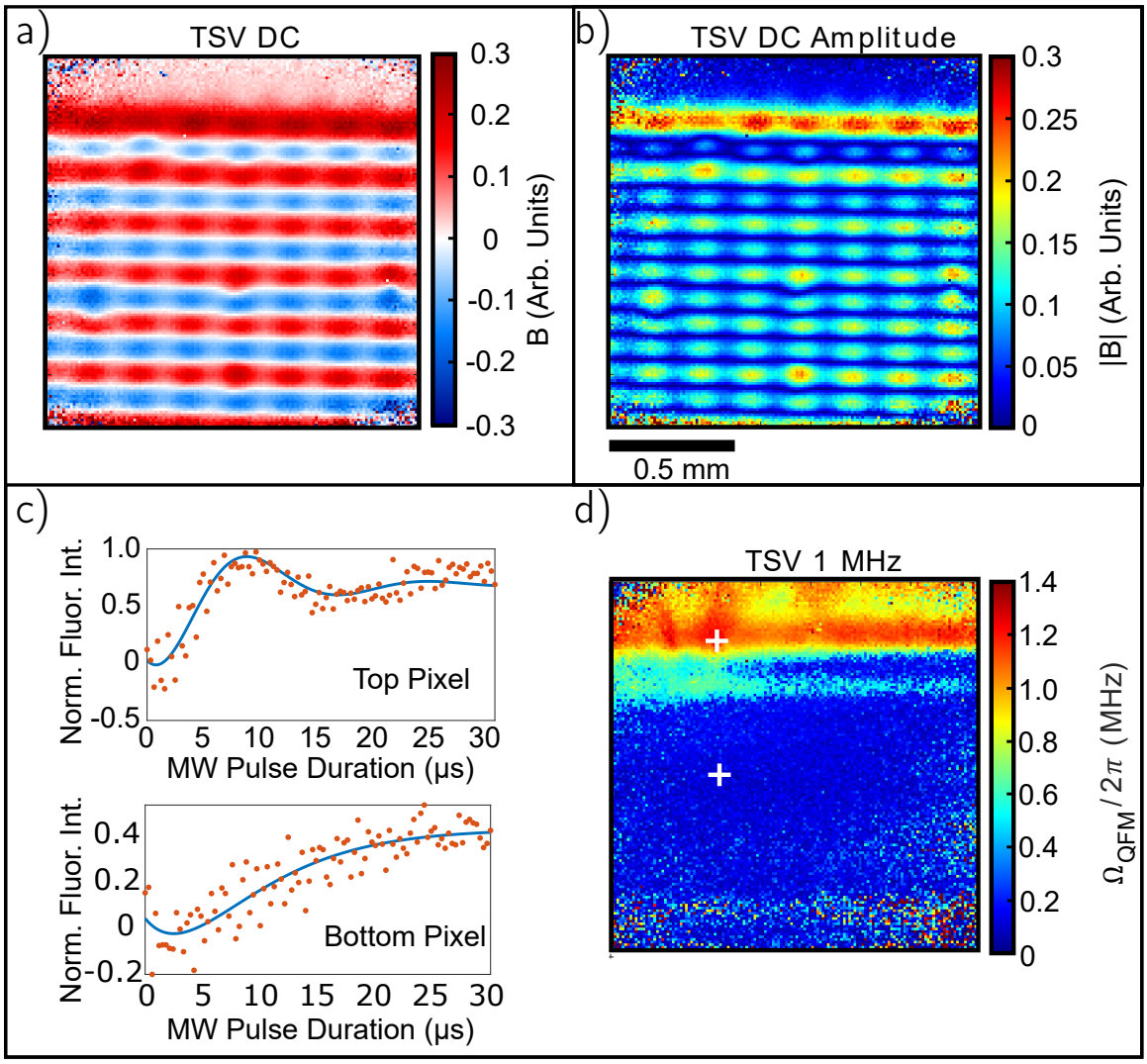

Figure 5-2: (a) The measured magnetic field projection along the diamond NV axis from the TSV test circuit when 5V DC is applied across its $\approx$ 17 kΩ resistance. (b) Absolute value of the magnetic image shown in a. (c) Rabi oscillations for two pixels in the $\omega_s = 2\pi\times1$ MHz AC magnetic image. (d) Detected Rabi frequencies using quantum frequency mixing for $\omega_s = 2\pi\times1$ MHz. The "hot spot" in the image indicates that a capacitive short is causing current to flow through a different section of the TSV structure than at DC signals.

Chapter 6

Conclusion and Outlook

In this thesis, we described the principles and methods for utilizing nitrogen-vacancy centers in a diamond lattice with appropriate quantum sensing protocols for high-resolution, wide field-of-view magnetic imaging across a range of signal frequencies. We then demonstrated an NV widefield magnetic imaging apparatus capable of measuring DC and AC magnetic fields up to 70 MHz over a 1.5×1.5 mm^2 field of view for various test structures. The imager itself overcomes several of the common challenges for NV pulsed magnetic imaging. After validating that the technique works with a simple straight-wire device, we then imaged an Archimedes spiral test structure and a fabricated through silicon via test chip.

We used a Rabi based magnetometry scheme with a linearly polarized signal and bias field to measure a signal field oscillating in the direction of the NV axis. Wang, *et al.* outlines additional protocols, including measuring with circularly polarized signal and bias fields or measuring in the transverse direction. Additional extensions could include applying spin-locking and pulsed dynamical decoupling methods such as CPMG [23].

Potential test devices to measure in the future include fractal antennas, and other passive RF components like a doubler or classical mixer. For example, QFM imaging could be used on a mixer to create a map of where exactly the current is going through the traces based on frequency. It could be potentially useful in analyzing abnormalities in RF devices or product inspection for mass produced circuits by

comparing the magnetic field map of a model circuit with a test device.

Future extensions of this work also include implementing a spectrum-analyzer imager (a form of hyperspectral imaging [30]), comparable to a scanning antenna measuring an electromagnetic power spectrum across a field of view [31]. Rather than raster-scanning an antenna to collect the spectrum from each pixel (which also requires frequency scanning from the spectrum analyzer), an NV-based QFM imager would instead scan ω_b (frequency scanning) and τ_{Rabi}, though we could avoid scanning τ_{Rabi} if using the $\pi/2$-pulse idea from Sec. 4.3.3. The resulting hyperspectral data cube could then be analyzed for PSA applications, such as counterfeit detection, component aging, and fabrication process variation over time or across a wafer [32, 33]. We note that previous works have also combined NV magnetic imaging with a spectrum analyzer [34, 35], but in these cases the imager itself is also the spectrum analyzer. This could be useful for validating how internal current paths within a device change as a function of frequency and impedance (for example, capacitive shorting). In addition, this apparatus and technique are well-suited for time-dependent imaging (i.e. magnetic movies), which can yield information of unintended frequency and amplitude variation over time.

This QFM imaging approach could be adapted for space-domain reflectometry for open-circuit fault localization. This was previously demonstrated with a scanning RF SQUID sensor [33], but could potentially achieve improved spatial resolution and sensitivity with an NV magnetic microscopy apparatus. Finally, this technique could be used to evaluate the RF and microwave images of hardware used for quantum computing, such as ion trap chips and superconducting qubits.

Appendix A

Magnetic Imager Noise and Resolution

A.1 Spatial Magnetic Noise Floor and Noise Subtraction Protocol

The spatial magnetic noise floor refers to the detected magnetic field difference between pixels when no signal is applied to the imager. The spatial magnetic noise floor and the per-pixel magnetic sensitivity determine whether a spatially varying signal can be resolved into an image [22]. We quantify the spatial magnetic noise floor as the standard deviation of magnetic-field measurements across a time-averaged image without external signals present. Uncorrelated spatial noise can be time averaged while correlated spatial magnetic noise limits the resolvable magnetic field. For example, fluctuations in laser power, vibration, and temperature induce changes in illumination intensity, the bias magnetic field, and the detuning of the system, all of which affect the NV precession rate [22, 36]. In order to mitigate the impact of spatially correlated noise varying slowly on the timescale between acquisitions of frame sets, we applied a noise subtraction protocol similar to one described in [22].

Figure A-1a demonstrates the background subtraction used for both on-resonance and QFM Rabi experiments. The MW drive is turned off every other pulse sequence.

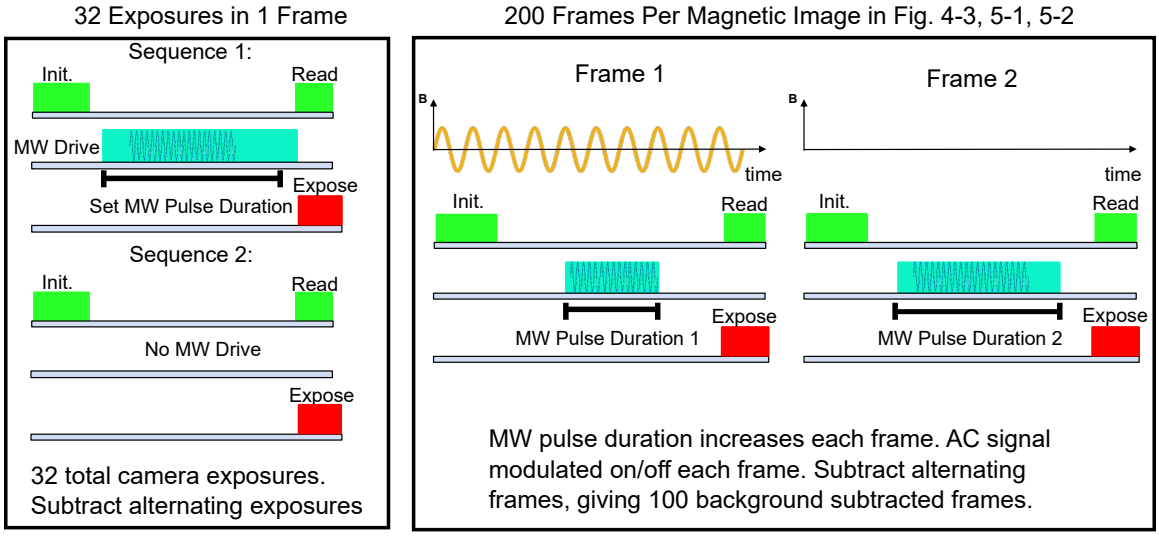

Figure A-1: (a) Visual depiction of how we perform the background subtraction for Rabi measurements. A pulse sequence repeats 32 times for each MW pulse duration. The MW drive is turned off every other sequence and the detected signal is subtracted from the previous sequence to provide the change in fluorescence caused by the MW drive. This removes non-magnetic noise from the system (b) Modulation of the QFM signal ω_s to remove magnetic noise. To create a magnetic image, we take a series of 200 frames where the signal is modulated on and off for alternating frames, with the "off" frame subtracted from the "on" frame. For each pixel, there is now a time trace of 100 points of background subtracted fluorescence caused by the QFM signal that can be plotted against the MW pulse duration length, from which the effective Rabi frequency can be extracted.

The DFPA has an in-pixel computational feature with an up-down counter for background subtraction [27]. In alternating exposures, the collected fluorescence from the "off" exposure is subtracted from the previous "on" exposure count, so only the change in fluorescence caused by the MW drive is counted. This removes non-magnetic background noise. The counts from 32 exposures are summed together and off-loaded onto the FPGA and to the computer via cameralink cables and a frame grabber as one "frame." We then repeat this process 200 times, increasing the MW pulse duration in each frame. For a QFM Rabi sequence, the QFM signal at frequency ω_s is modulated on and off in alternating frames with "off" frames subtracted from the "on" frames count in the post-acquisition analysis. (Technically, the subtracted background image should have the same MW pulse duration length, but since there is no applied signal, the bias is far off the QFM resonance for this background image, so in practice it does

not make a significant difference). This removes magnetic background noise. For each pixel, there is now a time trace of 100 points of background subtracted fluorescence counts caused by the QFM signal that can be plotted against the MW pulse duration length, from which the effective target Rabi frequency can be extracted. This entire process is repeated for a given amount of time and the fluorescence count values for each pulse duration time are averaged over the total number of iterations, giving the time-averaged Rabi oscillation. For the Rabi oscillations in Figs. 4-3 and 5-1, the fluorescence counts are normalized to each other for easy comparison.

For Ramsey DC measurements, we use a digital phase shifter to add a π phase shift on the second $\pi/2$ pulse of every other pulse sequence. This inverts the measured population difference of alternate exposures. We subtract alternating exposure counts and average the difference, then repeat this process for 32 total exposures and sum the fluorescence count, removing the non-magnetic background noise for a frame. We then repeat this process with a modulated current, taking the difference of alternating frames, with one frame having a positively applied current and another frame having a negatively applied current to remove magnetic background noise.

We calculate the spatial magnetic noise floor σ_{spatial} for different acquisition times with a method similar to calculating an Allan deviation [36]. We start with a set of m images collected over a period of time $\tau = \tau_1$ for each image with a total collection time $T = m\tau_1$ for the entire set of images. Then, we take the standard deviation of the pixel values in each image. Finally, we take the mean and standard error of this set of m standard deviations (the mean is the spatial magnetic noise floor value σ_{spatial} and the standard error gives error bars for σ_{spatial}). This σ_{spatial} tells us how much the pixel-to-pixel variation changes across time T for an image captured over time τ_1. To see how time averaging affects this pixel-to-pixel variation, we average the pixel values in images 1 and 2 and call that a new image 1 averaged over $\tau_2 = 2\tau_1$, average the pixel values in images 3 and 4 and call that image 2, and repeat this for all neighboring pairs in the set of m images. We then find the pixel-to-pixel standard deviations for this set of $m/2$ images and the mean and standard error for the set of standard deviations (which is σ_{spatial} and its error bars for τ_2). We repeat this for

integer multiples of τ_1 and then plot the σ_{spatial} values as a function of τ. This shows how long time averaging improves the pixel-to-pixel sensitivity. To see how time averaging affects the per-pixel sensitivity, we can perform a normal Allan deviation for each pixel [22].

Figure A-2 demonstrates the spatial magnetic noise floor for DC measurements as a function of acquisition time τ. The blue line shows the magnetic noise floor when no background frames are subtracted. The green line shows the magnetic noise floor when a single averaged background image is subtracted from each image. Both level out quickly with acquisition time, demonstrating where it is no longer beneficial to continue averaging the collected signal due to correlated noise. The black points represent the magnetic noise floor when alternate frames are subtracted. In signal processing, averaging n samples of uncorrelated noise reduces the noise level by $\sqrt{n}$. Since our acquisition time is proportional to the number of images collected and averaged, this translates to reduced noise $\propto \sqrt{\tau}$ for uncorrelated noise measurements. When we use our background subtraction scheme, σ_{spatial} as a function of acquisition time τ follows this expected power law scaling behavior $\propto \tau^{-\frac{1}{2}}$ shown in red [22, 36]. This indicates that our background subtraction scheme has removed correlated noise for at least 30 minutes of acquisition time, meaning we can continually average for at least 30 minutes to improve the magnetic noise floor for DC measurements. The magnetic noise floor could also be improved by binning the pixels (or increasing the pixel size) at the cost of spatial resolution [22]. Due to a calibration error, the images used were in approximate magnetic field units, within a factor of two of μT. A future extension of this work will include finding the spatial magnetic noise floor for AC measurements.

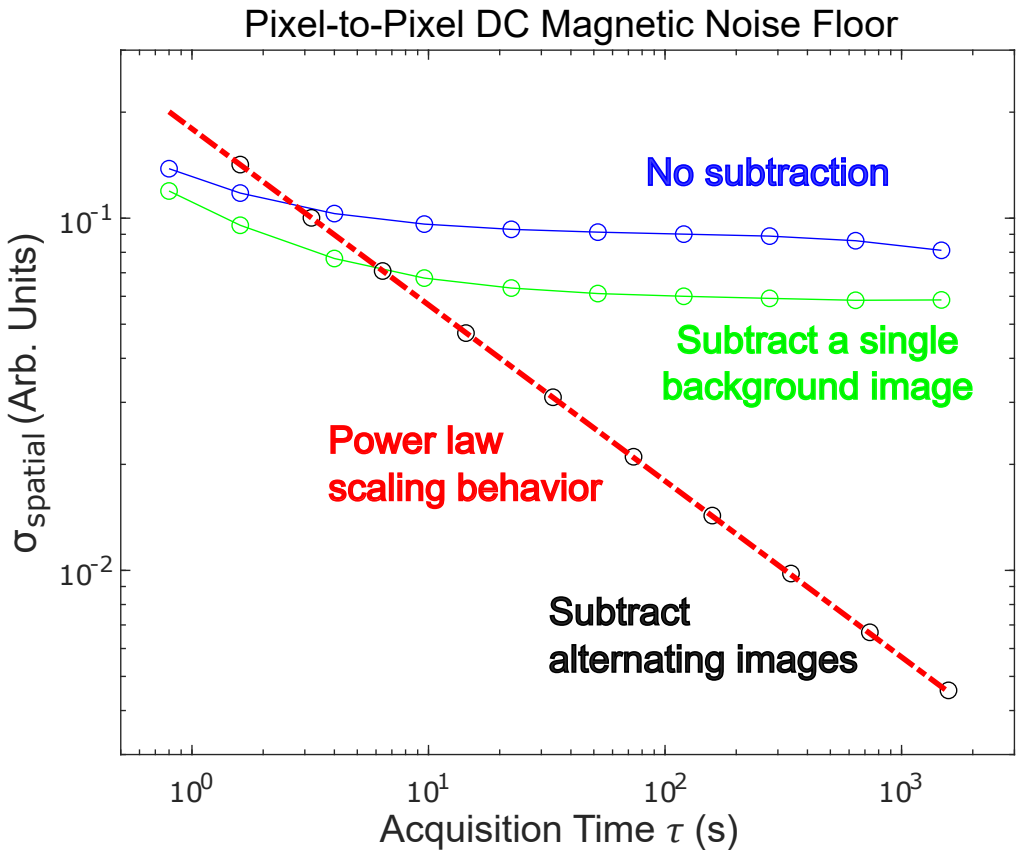

Figure A-2: Spatial magnetic noise floor σ_{spatial} as a function of acquisition time. The spatial magnetic noise floor represents the spread of magnetic field values across an image when no signal is present. The blue line shows the magnetic noise floor as a function of acquisition time when no background is subtracted. The green line shows when a single averaged background image is subtracted from each image. The black points show subtracted alternating images, which continually improves the magnetic noise floor by $\tau^{-\frac{1}{2}}$. Due to a calibration error, the values are in approximate magnetic units within a factor of two of μT. The error bars have been removed to simplify the image, but the standard errors for σ_{spatial} when subtracting alternating images are relatively small ($\sim 10^{-4}$ in the same units).

A.2 Resolution

A.2.1 Spatial Resolution

Spatial resolution refers to the smallest distinguishable unit that can be discerned with the magnetic imager. We have not yet characterized the spatial resolution of

the magnetic imager. This could be done by creating a meander line like that in A-3 and measuring the magnetic field to see which lines are individually discernible. The limit for the spatial resolution is primarily determined by the following as outlined in [5]:

- The stand-off distance, which refers to how far away the magnetic field created by the sample is from the NV centers.
- The NV layer thickness, which for our diamond is ∼20μm.
- The optical diffraction limit, which is set by the numerical aperture (NA) of the objective ($\lambda/(2NA)$). For our objective, the NA is 0.57.

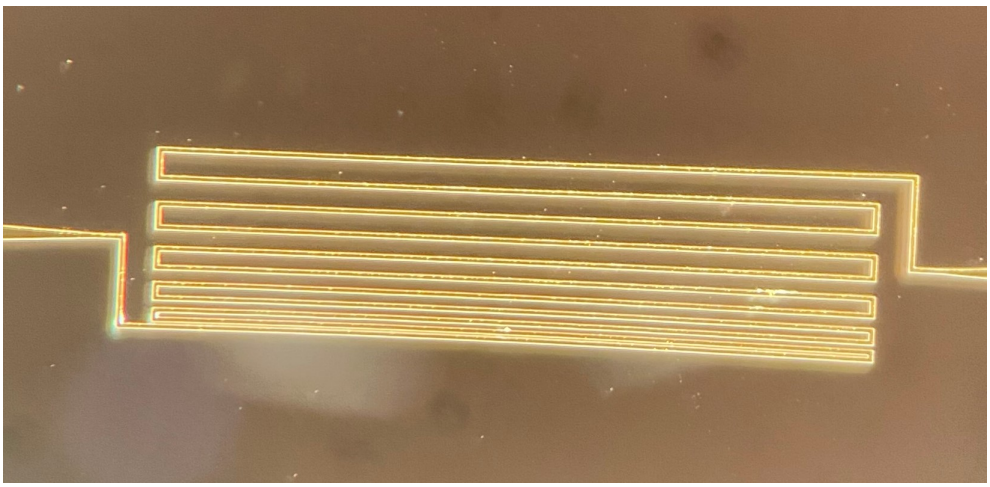

Figure A-3: Test structure that could be used to characterize the spatial resolution of the imager. Structure fabricated on sapphire printed circuit board with transmission line created by gold deposition process. The meander lines have a decreasing separation distance in intervals of 10 μm in order to demonstrate spatial resolution.

A.2.2 Temporal Resolution

The temporal resolution is the amount of time required between each measurement of a sample magnetic field. The physical limit for a magnetic imager using NV centers in diamond is on the order of ∼MHz, which is the time it takes NV centers to react to a change in the test field and is limited by the 1E metastable state lifetime [5]. In

practice, the limit is set by the signal-to-noise ratio, since a faster resolution means a limited amount of time to collect the signal. For example, for the TSV magnetic movie, for a temporal resolution of 1.5 ms, the SNR is sufficient to see the alternating current of the daisy chained structure, but the vertical movement of the trace in and out of the plane is not as clearly discernible.

Appendix B

Magnetic Imager Experimental Setup

B.1 Magnetic Imager Optical Path

The experimental setup begins with an 18 W 532 nm laser (Lighthouse photonics: Sprout-H). The laser beam passes through a reversed beam expander (Thorlabs) to reduce the beam size to 1/5 its original size, and is then focused into an acousto-optic modulator (AOMO 3250-220). The zeroth order beam is directed to a thermal heat sink by a D mirror (BBE02), and the first-order diffracted beam passes through a half-wave plate and a polarizing beam splitter (VAS-532), which are used to control the intensity and polarization axes of the light. Approximately 1 W passes through a collimating lens and reflects off two broadband dielectric mirrors while the remaining power is directed to a second heat sink. It passes through a 3× beam expander, after which it is passed through a holographic grating beam shaper (TH-248-Q-Y-A), which shapes the beam to provide uniformity across the diamond. The beam then passes through a focusing lens (750 mm) after which it is reflected off two additional broadband dielectric mirrors. It traverses through another half-wave plate to rotate the polarization vector appropriately onto the diamond. The beam then reflects off another broadband dielectric mirror and into the side of the diamond. Fluorescence from the diamond is collected by a low-magnification Zeiss objective with a focal length of 35.8 mm and numerical aperture of 0.57. The fluorescence then passes through a 100 mm tube lens (Spherical singlet B coated) 2 in. Any green light is then

filtered by a green laser light blocker (Semrock Edgefilter ∼635 nm) before being captured by the 256x256 pixel silicon digital focal plane array.

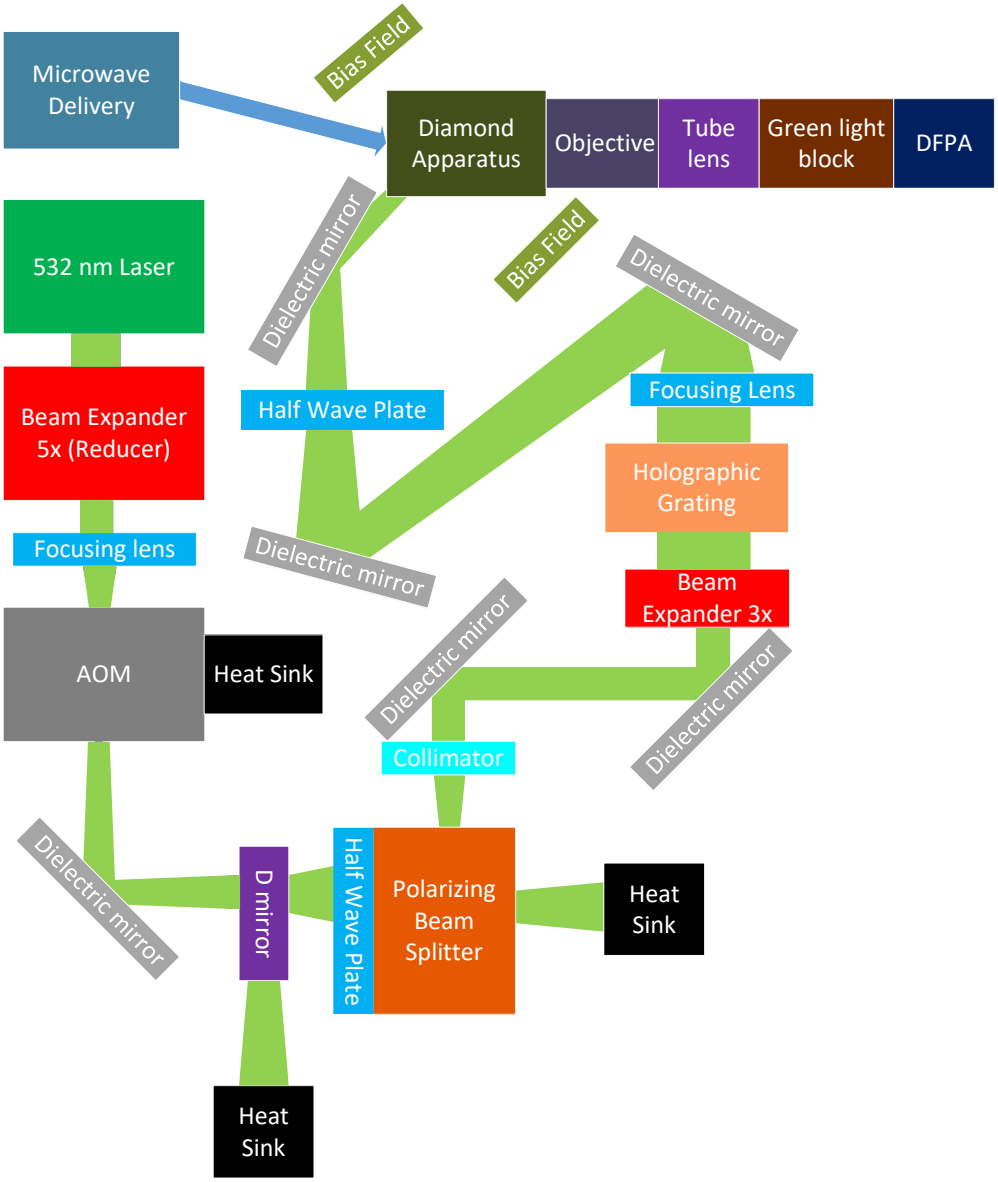

Figure B-1: Block diagram showing the excitation optical path.

B.2 Static Bias Magnetic Field

In order to create a Zeeman splitting sufficient to resolve the $m_s = -1$ and $m_s = +1$ states, a static bias field composed of two groups of eight magnetized cylindrical samarium cobalt permanent magnets arranged in an octagonal pattern equidistant on opposite sides of the diamond to create a homogeneous static magnetic field of approximately 1 mT aligned along one of the NV center axes.

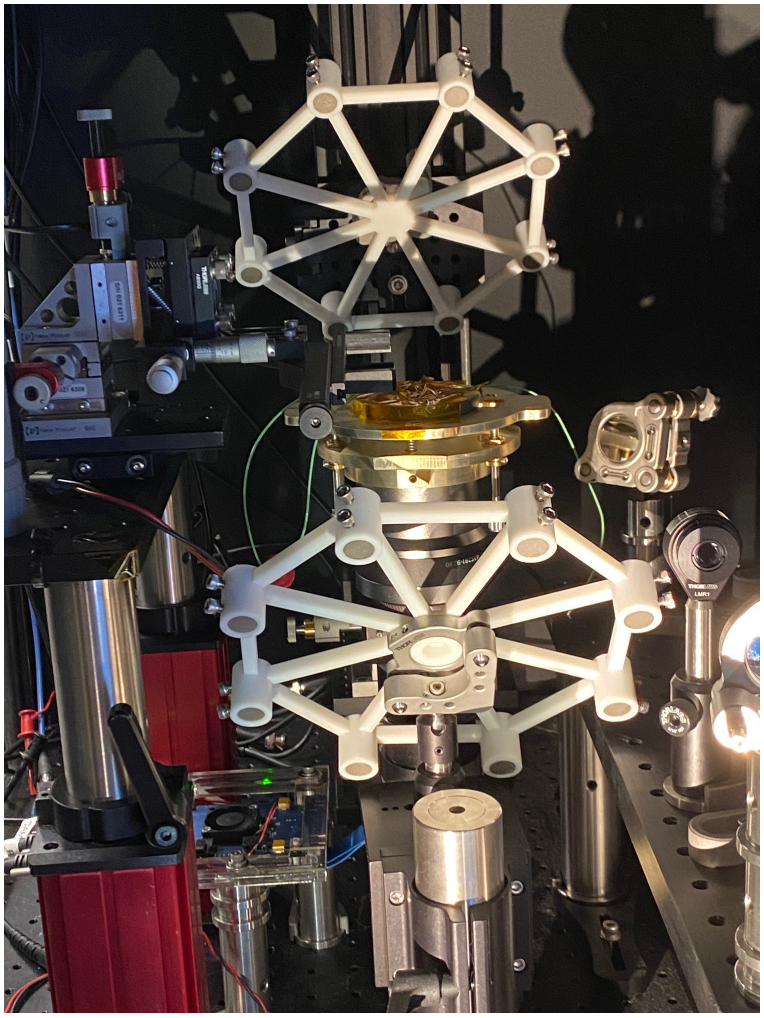

Figure B-2: Image of Bias Magnets. Eight circular ferromagnets are placed in an octagonal shape in a "Ferris Wheel" to create a homogeneous magnetic field centered along the [1,1,1] direction.

B.3 Experiment Pulse Sequences

A signal generator provides the triggering for the arbitrary waveform generator, with the repetition rate for the Ramsey experiments being 32 kHz (31.25 μs). The AWG controls the timing off the trigger and pulses for the laser, microwaves, digital phase shifters, and DC signal applied to the device. The on-resonance Rabi sequence used to check the Ramsey experiment has an initialization time of 2 μs, microwave pulse durations ranging from 50 ns to 9 μs, and a readout time of 8 μs, with the total sequence length lasting 20 μs. Although the initialization pulse for this sequence is short, the readout and initialization pulses occur in rapid succession, so the readout from the previous pulse ensures the state is already mostly in the $m_s = 0$ state when the sequence begins.

For the Ramsey experiment, the pulse sequence has an initialization time of 8μs, MW pulse durations of $\pi/2$ determined from the Rabi frequency (with a maximum alloted time of 500 ns), precession times up to 2 μs, and a readout time of 6 μs, with the total sequence lasting 20 μs. The initialization and readout times were chosen to improve the temporal resolution of the magnetic movie at the expense of fluorescence intensity. The sequence repeats for 32 exposures, after which there is 500 μs of dead time while the collected signal is off-loaded onto the FPGA and then to the computer via camera link cables and a frame grabber. This process repeats for 200 times, leading to a total experiment length of 0.3 s. We observe variable variable dead time after each experiment for data to be read from the frame grabber into the computer's acquisition software. The total acquisition time per image is $\sim$ 0.8s.

For the quantum frequency mixing Rabi experiment, the repetition rate for the experiment is 8 kHz (125 μs). The pulse sequence has an initialization time of 25 μs, MW pulse durations ranging from 50 ns to 31 μs, readout time of 8 μs, with the total sequence length lasting 65 μs. This sequence was used for both the on-resonance Rabi check and the actual QFM measurement. The initialization and readout times were chosen to maximize the fluorescence intensity. The sequence repeats for 32 exposures at each MW pulse duration, with 500 μs of dead time after each frame. This repeats

for each of the 200 steps of varying MW pulse durations, leading to a total experiment length of 0.9 s, with variable dead time in between each sequence making a total of ∼1.5 s per image. The total acquisition time for the time-averaged images in Fig. 4-3 and Fig. 5-1 is ∼5 minutes.

B.4 Electronics

B.4.1 Acousto-Optic Modulator Electronics

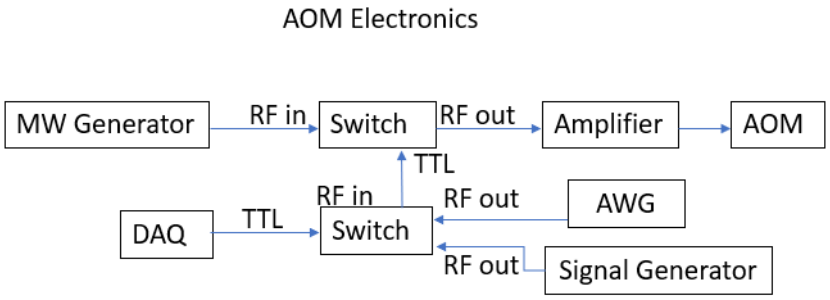

Figure B-3: Schematic of the electronics needed to control the AOM, which gates the laser and enables pulse sequencing.

Figure B-3 shows the electronics for controlling the acousto-optic modulator. A signal generator synthesizes the initial 250 MHz RF signal and passes it to a switch, which gates it by a transistor-transistor-logic (TTL) signal from the AWG according to the pulse sequence needed for the experiment. It then passes to an amplifier before being sent to a piezoelectric transducer in the AOM, which oscillates a crystal, generating sound waves that diffract the laser beam [37]. After 200 frames, data is transferred to the computer for a variable amount of dead time, during which a National Instruments DAQ interrupts the master trigger signal to the AWG, and it does not output waveforms. Since we want the AOM to continue running during this interruption to reduce thermal fluctuations and keep a consistent temperature between image acquisitions, we also have the DAQ send a TTL signal to switch the signal from the AWG to a separate signal generator, which continues applying gated pulses to the AOM.

B.4.2 Microwave Electronics

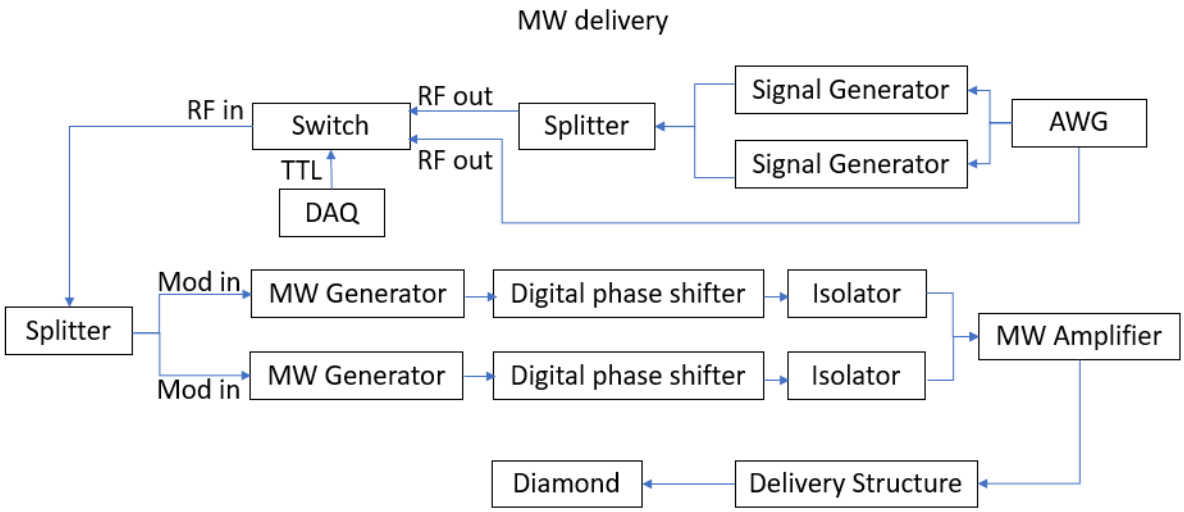

Figure B-4: Schematic of the electronics used to deliver microwaves to the diamond.

Figure B-4 shows the MW delivery electronics for both Rabi and Ramsey measurements. For a Ramsey measurement, the AWG outputs the Ramsey $\pi/2$ pulse triggers to two signal generators, which generate the pulse gate signals for the MW $\pi/2$ pulses. This configuration allows for the pulse durations to be controlled without modifying the AWG waveforms. These are combined using an RF power combiner. A switch, controlled by the DAQ, determines whether these Ramsey control signals pass through to the MW generators, or whether Rabi pulses generated by the AWG for Rabi sequences pass through. The signals are then split with another RF power splitter and are used to modulate two MW generators. The MW generators output a resonant frequency signal for the $m_s = +1$ and $m_s = -1$ states respectively for a double quantum Ramsey sequence. For a single quantum sequence, only one MW generator is used. Each MW generator passes the signals through a digital phase shifter and isolator to control the phase and reduce noise for the signal. The signals are then combined and amplified before being passed to the MW delivery structure, which creates a uniform MW field across the diamond. For a Rabi measurement, the AWG outputs a pulse gate signal directly to the switch and only utilizes one of the MW generators (which outputs a resonant frequency signal for normal Rabi and ω_b

frequency signal for QFM Rabi experiments). For a QFM experiment with a $\pi/2$ pulse for the slope detection scheme described in Sec. 4.3.3, the AWG could send a $\pi/2$ pulse trigger to another signal generator (not depicted) to generate the pulse gate signal for the QFM $\pi/2$ pulse. It would then pass through the switch controlled by the DAQ and modulate the other MW generator. The MW generator would output the resonant frequency signal, which would follow the same steps as the other experiments to reach the diamond.

B.4.3 Signal Electronics

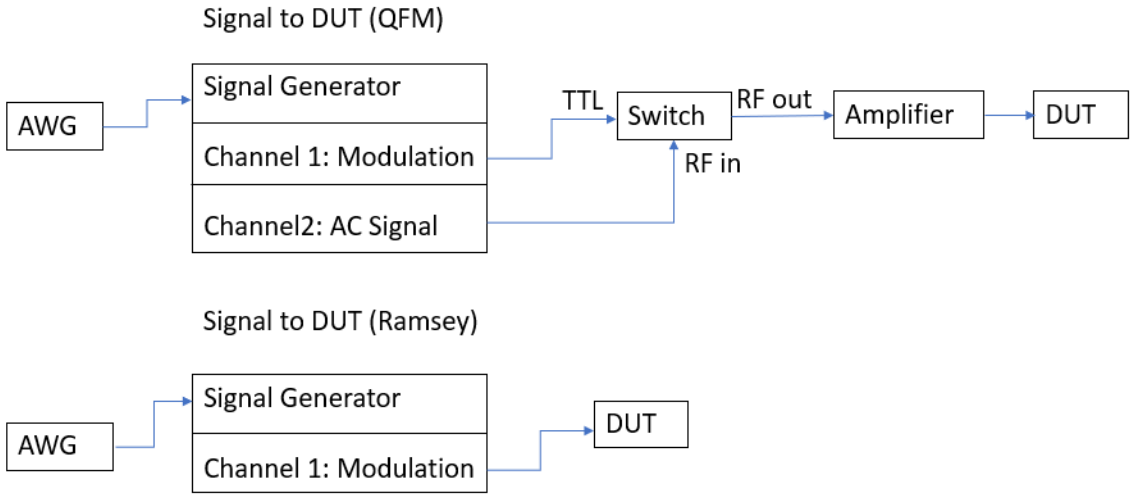

Figure B-5: Schematic of the electronics used to deliver the sensing signal to the device under test (DUT).

Figure B-5 shows the electronics for delivering the signals to be sensed to the DUT for both Rabi and Ramsey measurements. For a QFM Rabi measurement, the AWG provides the external trigger for a signal generator to synchronize it with the repetition rate of the experiment. Channel one of the signal generator outputs the modulating sequence for background subtraction. It provides TTL to a switch to gate the AC signal. For our experiment, the modulating signal has a period of 9 ms with a 50% duty cycle to synchronize with alternating frames, with a ~150 cycle burst to keep a constant MW power delivered to the diamond even during the 500 µs dead time periods when frames are being read out to keep a constant temperature without

missing the next trigger. Channel 2 outputs the desired signal at frequency ω_s to be sensed, which is gated by the switch, amplified, and sent to the DUT. For Ramsey signals, the modulated signal is passed directly to the DUT. For our DC experiments, the signal has a 3 ms period with a 50% duty cycle and a 255 burst cycle count. The high and low levels for the applied signal were the desired positive and negative values to create the desired current. For a 1 mA DC current, we applied ± 25 mV across a $\sim 50\Omega$ load.

B.4.4 Arbitrary Waveform Generator Setup Summary

Channel 1 Marker 1	AOM Pulse Gate
Channel 1 Marker 2	1^{st} Ramsey $\pi/2$ Pulse Trigger
Channel 2 Marker 1	Rabi Trigger
Channel 2 Marker 2	Digital Phase Shifter Trigger
Channel 3 Marker 1	Sequence Start Trigger
Channel 3 Marker 2	Signal to DUT Trigger
Channel 4 Marker 1	2^{nd} Ramsey $\pi/2$ Pulse Trigger
Channel 4 Marker 2	DFPA Trigger
Trigger Input	DAQ

Table B.1: Table summarizing each channel of the arbitrary waveform generator and the section of the experiment it controls. For a QFM experiment, Channel 1 Marker 2 can be re-purposed to provide the QFM $\pi/2$ pulse trigger.

B.4.5 Electronics Components List

AWG	AWG 5014 C TekTronix
Signal Generator	Keysight 33600A
Power Supply	Rigol DP 832, DP 811
MW Delivery	Stanford Research Systems SG384, SG396
AOM Amplifier	Minicircuits ZHL-20 W-13+
RF Amplifier	Minicircuits LZY-22+
MW Amplifier	Minicircuits ZHL-16W-43-S+
Switch	Minicircuits ZASWA-2-50DR+
Isolator	Aerotek E60-1FFF
Digital Phase Shifter	Analog Devices HMC647ALP6E
DAQ	National Instruments DAQ USB-6363

Table B.2: List of electronics components used for this experiment

Bibliography

[1] C. L. Degen, F. Reinhard, and P. Cappellaro. Quantum sensing. *Rev. Mod. Phys.*, 89:035002, Jul 2017.

[2] Nabeel Aslam, Hengyun Zhou, Elana K. Urbach, Matthew J. Turner, Ronald L. Walsworth, Mikhail D. Lukin, and Hongkun Park. Quantum sensors for biomedical applications. *Nature Reviews Physics*, 5:157–169, Mar 2023.

[3] Jennifer M. Schloss, John F. Barry, Matthew J. Turner, and Ronald L. Walsworth. Simultaneous broadband vector magnetometry using solid-state spins, 2018.

[4] Romana Schirhagl, Kevin Chang, Michael Loretz, and Christian L. Degen. Nitrogen-vacancy centers in diamond: Nanoscale sensors for physics and biology. *Annual Review of Physical Chemistry*, 65(1):83–105, 2014.

[5] Edlyn V Levine, Matthew J Turner, Pauli Kehayias, Connor A Hart, Nicholas Langellier, Raisa Trubko, David R Glenn, Roger R Fu, and Ronald L Walsworth. Principles and techniques of the quantum diamond microscope. *Nanophotonics*, 8(11):1945–1973, 2019.

[6] S. C. Scholten, A. J. Healey, I. O. Robertson, G. J. Abrahams, D. A. Broadway, and J.-P. Tetienne. Widefield quantum microscopy with nitrogen-vacancy centers in diamond: Strengths, limitations, and prospects. *Journal of Applied Physics*, 130(15):150902, 2021.

[7] Sean M. Oliver, Dmitro J. Martynowych, Matthew J. Turner, David A. Hopper, Ronald L. Walsworth, and Edlyn V. Levine. Vector Magnetic Current Imaging of an 8 nm Process Node Chip and 3D Current Distributions Using the Quantum Diamond Microscope. In *International Symposium for Testing and Failure Analysis*, pages 96–107, 10 2021.

[8] L M Pham, D Le Sage, P L Stanwix, T K Yeung, D Glenn, A Trifonov, P Cappellaro, P R Hemmer, M D Lukin, H Park, A Yacoby, and R L Walsworth. Magnetic field imaging with nitrogen-vacancy ensembles. *New Journal of Physics*, 13(4):045021, 2011.

[9] Stephen J. DeVience, Linh M. Pham, Igor Lovchinsky, Alexander O. Sushkov, Nir Bar-Gill, Chinmay Belthangady, Francesco Casola, Madeleine Corbett, Huiliang

Zhang, Mikhail Lukin, Hongkun Park, Amir Yacoby, and Ronald L. Walsworth. Nanoscale NMR spectroscopy and imaging of multiple nuclear species. *Nature Nanotechnology*, 10:129–134, 2015.

[10] Andrew Horsley, Patrick Appel, Janik Wolters, Jocelyn Achard, Alexandre Tallaire, Patrick Maletinsky, and Philipp Treutlein. Microwave Device Characterization Using a Widefield Diamond Microscope. *Phys. Rev. Applied*, 10:044039, Oct 2018.

[11] F. Ziem, M. Garsi, H. Fedder, and J. Wrachtrup. Quantitative nanoscale MRI with a wide field of view. *Scientific Reports*, 9(1):12166, Aug 2019.

[12] Karl D. Briegel, Nick R. von Grafenstein, Julia C. Draeger, Peter Blumler, Robin D. Allert, and Dominik B. Bucher. Optical widefield nuclear magnetic resonance microscopy. *arXiv:2402.18239*, 2024.

[13] J-M Cai, B Naydenov, R Pfeiffer, L P McGuinness, K D Jahnke, F Jelezko, M B Plenio, and A Retzker. Robust dynamical decoupling with concatenated continuous driving. *New Journal of Physics*, 14(11):113023, 2012.

[14] Scott T. Alsid, Jennifer M. Schloss, Matthew H. Steinecker, John F. Barry, Andrew C. Maccabe, Guoqing Wang, Paola Cappellaro, and Danielle A. Braje. Solid-state microwave magnetometer with picotesla-level sensitivity. *Phys. Rev. Appl.*, 19:054095, May 2023.

[15] Guoqing Wang, Yi-Xiang Liu, Jennifer M. Schloss, Scott T. Alsid, Danielle A. Braje, and Paola Cappellaro. Sensing of arbitrary-frequency fields using a quantum mixer. *Phys. Rev. X*, 12:021061, Jun 2022.

[16] Ronald M. Jones, Dieter Gerlich, and Scott L. Anderson. Simple radio-frequency power source for ion guides and ion traps. *Review of Scientific Instruments*, 68(9):3357–3362, 09 1997.

[17] Marcus W Doherty, Neil B Manson, Paul Delaney, Fedor Jelezko, Jorg Wrachtrup, and Lloyd C L Hollenberg. The nitrogen-vacancy colour centre in diamond. *Physics Reports*, 528(1):1 – 45, 2013.

[18] M. W. Doherty, F. Dolde, H. Fedder, F. Jelezko, J. Wrachtrup, N. B. Manson, and L. C. L. Hollenberg. Theory of the ground-state spin of the nv- center in diamond. *Phys. Rev. B*, 85:205203, May 2012.

[19] S. Felton, A. M. Edmonds, M. E. Newton, P. M. Martineau, D. Fisher, and D. J. Twitchen. Electron paramagnetic resonance studies of the neutral nitrogen vacancy in diamond. *Phys. Rev. B*, 77:081201, Feb 2008.

[20] John F. Barry, Jennifer M. Schloss, Erik Bauch, Matthew J. Turner, Connor A. Hart, Linh M. Pham, and Ronald L. Walsworth. Sensitivity optimization for nv-diamond magnetometry. *Rev. Mod. Phys.*, 92:015004, Mar 2020.

[21] J. J. Sakurai and Jim Napolitano. *Modern Quantum Mechanics*. Cambridge University Press, 3 edition, 2020.

[22] Jiashen Tang, Zechuan Yin, Connor A. Hart, John W. Blanchard, Jner Tzern Oon, Smriti Bhalerao, Jennifer M. Schloss, Matthew J. Turner, and Ronald L. Walsworth. Quantum diamond microscope for dynamic imaging of magnetic fields. *AVS Quantum Science*, 5(4):044403, 11 2023.

[23] Guoqing Wang, Yi-Xiang Liu, Jennifer M. Schloss, Scott T. Alsid, Danielle A. Braje, and Paola Cappellaro. Sensing of arbitrary-frequency fields using a quantum mixer. *Phys. Rev. X*, 12:021061, Jun 2022.

[24] S. A. Maas. *Microwave mixers*. 1986.

[25] M. W. Doherty, V. M. Acosta, A. Jarmola, M. S. J. Barson, N. B. Manson, D. Budker, and L. C. L. Hollenberg. Temperature shifts of the resonances of the nv- center in diamond. *Phys. Rev. B*, 90:041201, Jul 2014.

[26] V. M. Acosta, E. Bauch, M. P. Ledbetter, A. Waxman, L.-S. Bouchard, and D. Budker. Temperature dependence of the nitrogen-vacancy magnetic resonance in diamond. *Phys. Rev. Lett.*, 104:070801, Feb 2010.

[27] Kenneth I Schultz, Michael W Kelly, Justin J Baker, Megan H Blackwell, Matthew G Brown, Curtis B Colonero, Christopher L David, Brian M Tyrrell, and James R Wey. Digital-pixel focal plane array technology. *Lincoln Laboratory Journal*, 20(2):36–51, 2014.

[28] Connor A. Hart, Jennifer M. Schloss, Matthew J. Turner, Patrick J. Scheidegger, Erik Bauch, and Ronald L. Walsworth. N-v–diamond magnetic microscopy using a double quantum 4-ramsey protocol. *Phys. Rev. Appl.*, 15:044020, Apr 2021.

[29] Erik Bauch, Connor A. Hart, Jennifer M. Schloss, Matthew J. Turner, John F. Barry, Pauli Kehayias, Swati Singh, and Ronald L. Walsworth. Ultralong dephasing times in solid-state spin ensembles via quantum control. *Phys. Rev. X*, 8:031025, Jul 2018.

[30] Nathan A. Hagen and Michael W. Kudenov. Review of snapshot spectral imaging technologies. *Optical Engineering*, 52(9):090901, 2013.

[31] Karynn A Sutherlin. Investigation of electromagnetic signatures of a fpga using an aprel em-isight system. Master's thesis, Air Force Institute of Technology, 2015.

[32] Paiboon Tangyunyong, Jr. Cole, Edward I., Guillermo M. Loubriel, Joshua Beutler, Darlene M. Udoni, Biliana S. Paskaleva, and Thomas E. Buchheit. Power Spectrum Analysis. In *International Symposium for Testing and Failure Analysis*, pages 73–78, 11 2017.

[33] Jan Gaudestad, Vladimir Talanov, Nicolas Gagliolo, and Antonio Orozco. Space domain reflectometry for open failure localization. In *2012 19th IEEE International Symposium on the Physical and Failure Analysis of Integrated Circuits*, pages 1–5, 2012.

[34] M. Chipaux, L. Toraille, C. Larat, L. Morvan, S. Pezzagna, J. Meijer, and T. Debuisschert. Wide bandwidth instantaneous radio frequency spectrum analyzer based on nitrogen vacancy centers in diamond. *Applied Physics Letters*, 107(23), 2015.

[35] Simone Magaletti, Ludovic Mayer, Jean-François Roch, and Thierry Debuisschert. A quantum radio frequency signal analyzer based on nitrogen vacancy centers in diamond. *Communications Engineering*, 1(1):19, Jul 2022.

[36] D. R. Glenn, R. R. Fu, P. Kehayias, D. Le Sage, E. A. Lima, B. P. Weiss, and R. L. Walsworth. Micrometer-scale magnetic imaging of geological samples using a quantum diamond microscope. *Geochemistry, Geophysics, Geosystems*, 18(8):3254–3267, 2017.

[37] Daniel J McCarron. A guide to acousto-optic modulators. 2007.